

Investigation into the extrudability of a new Mg-Al-Zn-RE alloy with large amounts of alloying elements

Bai, Sheng Wen; Fang, Gang; Zhou, Jie

DOI

[10.1007/s11661-019-05242-9](https://doi.org/10.1007/s11661-019-05242-9)

Publication date

2019

Document Version

Accepted author manuscript

Published in

Metallurgical and Materials Transactions A: Physical Metallurgy and Materials Science

Citation (APA)

Bai, S. W., Fang, G., & Zhou, J. (2019). Investigation into the extrudability of a new Mg-Al-Zn-RE alloy with large amounts of alloying elements. *Metallurgical and Materials Transactions A: Physical Metallurgy and Materials Science*, 50(7), 3246-3264. <https://doi.org/10.1007/s11661-019-05242-9>

Important note

To cite this publication, please use the final published version (if applicable).
Please check the document version above.

Copyright

Other than for strictly personal use, it is not permitted to download, forward or distribute the text or part of it, without the consent of the author(s) and/or copyright holder(s), unless the work is under an open content license such as Creative Commons.

Takedown policy

Please contact us and provide details if you believe this document breaches copyrights.
We will remove access to the work immediately and investigate your claim.

1 **Investigation into the extrudability of a new Mg-Al-Zn-RE**
2 **alloy with large amounts of alloying elements**

3 Sheng-Wen Bai¹, Gang Fang^{1, *}, Jie Zhou²

4 ¹ State Key Laboratory of Tribology, Department of Mechanical Engineering, Tsinghua
5 University, Beijing 100084, China

6 ² Department of Biomechanical Engineering, Delft University of Technology, Mekelweg 2,
7 2628 CD Delft, The Netherlands

8 *Corresponding author, Gang Fang: Tel: +86-10-6278 2694, E-mail: fangg@tsinghua.edu.cn

9
10 **Abstract**

11 The present study was aimed to determine the extrudability of a newly developed
12 Mg-Al-Zn-RE magnesium alloy with large amounts of alloying elements. The
13 experimental and numerical investigation clearly showed that the extrudate
14 temperature was a crucial factor deciding if a critical temperature between 754 K and
15 768 K (481 °C and 495 °C) was reached during extrusion, above which hot shortness
16 occurred. Under the extrusion conditions applied, dynamic recrystallization (DRX)
17 occurred, leading to grain refinement from a mean grain size of 165 μm in the
18 as-solid-solution-treated billet to 8.0-10.9 μm in the extruded rods. Second-phase
19 particles, such as Mg₁₇Al₁₂ and Al₁₁La₃, were found to distribute on grain boundaries
20 and aid in grain refinement. The mechanical properties of the extrudate were greatly
21 influenced by the as-extruded microstructure and extrusion condition. As the initial

22 billet temperature decreased, the ultimate tensile strength (UTS) and elongation of the
23 alloy increased, while yield strength (YS) remained almost unchanged. At an initial
24 billet temperature of 523 K (250 °C), a stem speed of 3.93 mm/s and a reduction ratio
25 of 29.8, the extruded magnesium alloy had a mean grain size of 8.0 μm. Its YS, UTS
26 and elongation reached 217 ± 3 MPa, 397 ± 7 MPa and $20 \pm 1.3\%$, respectively.

27 **Keywords:** magnesium; extrusion; microstructure; mechanical property; hot shortness

28

29 **1. Introduction**

30 Since the beginning of this century, magnesium alloys, the lightest structural metallic
31 materials, have attracted great attention for applications in 3-C (computers,
32 communications and consumer electronics) products, automobiles and aerospace in
33 order to realize weight reduction [1-6]. Cast magnesium alloy parts made by using a
34 variety of casting techniques have been widely accepted for these applications [7].
35 However, the applications of wrought magnesium alloys have been rather limited,
36 although in general wrought magnesium alloys possess better mechanical properties
37 than the cast counterpart and are thus more suitable for structural applications [8-9].
38 Extruded magnesium alloy products, for example, accounted for less than 3% of the
39 annual output of magnesium production in 2013 [10]. The limited applications of
40 extruded products are mainly due to the low extrudability of magnesium alloys,
41 compared to aluminum alloys, leading to low productivity and low cost-effectiveness.

42 The limited use of extruded magnesium alloy products is also due to the achievable
43 mechanical properties that are not substantially better than those of the cast
44 counterpart. In recent years, a lot of research efforts have been made to improve the
45 mechanical properties and extrudability of magnesium alloys.

46

47 Basically, there are two ways to improve the mechanical properties of extruded
48 magnesium alloys. Alloying is effective in enhancing the mechanical properties of
49 magnesium, but at the same time imposes limitations to applicable extrusion speed, as
50 a result of raised resistance to hot deformation, increased temperature rise during the
51 process and lowered incipient melting point. Microstructure control throughout
52 materials processing from casting to extrusion is also effective, especially the control
53 of grain structure within an applicable extrusion process window by applying an
54 optimum combination of extrusion process parameters. Obviously, it is the best if
55 alloying and microstructure control are combined to achieve optimum mechanical
56 properties from a refined grain structure and from the distribution of fine precipitates
57 at a minimum loss in extrusion speed.

58

59 The effect of alloying on the microstructure, extrudability and mechanical properties
60 of extruded magnesium alloy products depends on the amount of a chosen element
61 and its solubility in the magnesium matrix. When its content is low, it stays dissolved
62 in the magnesium matrix even at room temperature, creating a solid solution

63 strengthening effect. However, when the content exceeds its solubility in the
64 magnesium matrix, second-phase particles precipitate as temperature decreases,
65 creating a precipitation strengthening effect and possibly contributing to a refined
66 grain structure as well by pinning grain boundaries, which in turn strengthens the
67 alloy further. These strengthening mechanisms may operate individually or in
68 combination. The mechanical properties of extruded magnesium were, for example,
69 shown to be improved through the addition of Al and Zn by a combination of
70 strengthening mechanisms, depending on the contents of these elements [11]. Yin et al.
71 [12] found that the addition of Zn refined the grain structure of an extruded
72 Mg-Zn-Mn alloy and led to an improved yield strength. In Mg-5Sn- x Zn alloys ($x=1,$
73 2, 4), the amounts of Mg₂Sn and MgZn particles increased with increasing Zn content,
74 which contributed to the mechanical properties of the extruded magnesium alloys
75 through precipitation strengthening [13]. Small amounts of Ca were found to be able
76 to refine the grain structure and improve both the tensile strength and elongation of
77 Mg-Al-Zn and Mg-Zn alloys [14, 15]. Rare earth (RE) elements, such as Gd, Y and
78 Ce, were added to different extruded magnesium alloys to enhance their mechanical
79 properties [16-21]. For example, Y improved the mechanical properties of Mg-Zn-Zr
80 alloys through grain refinement and the formation of the I-phase (Mg₃Zn₆Y).
81 However, an excessive addition of Y to the alloys led to the formation of the W-phase
82 (Mg₃Zn₃Y₂), which decreased the strengths. Actually, it is the ratio of Y to Zn (wt. %)
83 that determines the volume fraction of the I-phase and its strengthening effect [18].

84 Zeng et al. [22] also demonstrated that the polygon-shaped Mg_3Zn_6Y phase played an
85 important role in strengthening the extruded magnesium alloy Mg-6Zn-1.5Y-0.5Zr.
86 Stanford et al. [23] found that the strength of magnesium was greatly improved by
87 adding 0.22-4.65% Gd, owing to the mechanisms of recrystallized grain refinement
88 and solution strengthening. Zhang et al. [24] revealed that the synthetic additions of
89 Ca, Ce and La to the Mg-6.0Zn alloy resulted in the refinement of secondary phases
90 and precipitates, promoting the pinning effect to restrict grain growth and the
91 dispersion strengthening effect. Homma et al. [25] developed a high-strength
92 magnesium alloy Mg-1.8Gd-1.8Y-0.7Zn-0.2Zr with an ultimate tensile strength (UTS)
93 of 542 MPa and a 0.2% proof stress of 473 MPa. The high strengths were achieved
94 thanks to fine precipitates formed during aging subsequent to hot extrusion. Yamasaki
95 et al. [26] found that the yield strength of the warm-extruded magnesium alloy
96 Mg-Zn-2.5Gd reached a high level of 345 MPa, because of the refinement of grains
97 and the dispersion of a precipitate with a long period ordered (LPO) structure. Chen et
98 al. [27] investigated the effect of Nd addition on the microstructures and mechanical
99 properties of the Mg-6Al-2Ca-xNd ($x=0, 1, 2, 3, 4$ and 5 wt.%) alloys. With
100 increasing content of Nd, the amounts of Al_2Nd and Al_3Nd phases increased, while
101 the amount of $Mg_{17}Al_{12}$ decreased. The presence of the Al-Nd compounds contributed
102 to the refinement of the recrystallized grain structure formed during hot extrusion,
103 leading to an enhanced yield strength. Therefore, it is critically important to

104 understand the strengthening phase formed in RE-containing magnesium alloys and
105 its sizes, volume fraction and distribution.

106

107 On the other hand, as mentioned earlier, with the addition of alloying elements to
108 magnesium, the extrudability usually decreases [11]. Luo et al. [28], for example,
109 found that the incipient melting point of the magnesium alloy AZ31 was 371 K (98 °C)
110 lower than that of AM30 due to the presence of Zn in the former. It means that AZ31
111 is more susceptible to hot shortness. To prevent hot shortness from occurring, a lower
112 initial billet temperature must be considered, if extrusion speed and reduction ratio are
113 desired to be fixed. As a result, the extrusion pressure required for the process will be
114 higher. If the force capacity of the available extrusion press is not enough, extrusion
115 speed or reduction ratio must be reduced in order to lower the pressure requirement,
116 leading to sacrifice in extrusion productivity. In the case of high-strength magnesium
117 alloys with large amounts of alloying elements, more severe limitations are imposed
118 on the applicable extrusion conditions. For each alloy, its extrusion window must be
119 specifically defined in order to avoid hot shortness and achieve the highest possible
120 extrusion productivity in combination with the consideration on the microstructure
121 and mechanical properties desired to achieve.

122

123 During hot extrusion, the main process parameters, i.e., initial billet temperature,
124 extrusion speed and reduction ratio, may all influence the microstructure of an

125 extruded magnesium alloy. The mechanical properties of the alloy depend on its
126 microstructural characteristics, such as grain size, the intensity of texture and the
127 distribution of second-phase particles [29-33]. Murai et al. [29] found that fine grains
128 in the extruded magnesium alloy AZ31 were obtained at a low initial billet
129 temperature and a low extrusion speed, resulting in high mechanical properties of the
130 extrudate. Ishihara et al. [30] reported that at a given initial billet temperature of 693
131 K (420 °C) and extrusion speed of 5 m/min, the mean grain size of the extruded
132 magnesium alloy AZ31 increased from 30 to 170 μm , when reduction ratio was
133 increased from 10 to 100. Zhang et al. [31] investigated the effect of the initial billet
134 temperature on the microstructure and mechanical properties of the extruded
135 Mg-1.0Zn-0.5Ca alloy. They found that with decreasing initial billet temperature from
136 673 K to 603 K (400 °C to 330 °C), the mean grain size decreased from 25 to 2.5 μm
137 and the ultimate tensile strength (UTS) increased from 201 to 300 MPa. Tong et al.
138 [32] found that the basal texture of the Mg-5.3Zn-0.6Ca alloy was weakened at a
139 higher extrusion speed, which resulted in a lower tensile yield strength. Park et al. [33]
140 demonstrated that the temperature rise occurring during extrusion increased the
141 solubility of Sn in the magnesium matrix and thereby reduced the volume fraction of
142 Mg_2Sn precipitates in the Mg-Sn-Al-Zn extrudate, resulting in a low strength.
143 Therefore, the choice of extrusion parameters is of critical importance for the
144 achievable mechanical properties of an extruded magnesium alloy.

145

146 Indeed, many of recent research efforts have aimed at achieving the highest possible
147 strength through optimizing extrusion condition, often in combination with
148 modification of alloy composition. By performing extrusion at an extrusion ratio of 44,
149 a ram speed of 60 mm/min and billet temperature of 623 K (350 °C), for example,
150 Shahzad et al. [34] obtained the ultimate tensile strength (UTS) of 328 MPa for the
151 magnesium alloy AZ80. Chen et al. [35] found that the UTS of the extruded
152 magnesium alloy Mg-5.3Zn-1.13Nd-0.51La-0.28Pr-0.79Zr could reach 325-350 MPa,
153 when the billet temperature applied was 523 K (250 °C). Singh et al. [36] developed
154 the extruded magnesium alloys Mg-6xZn-xY ($x=0.2, 0.35$ and 0.5 at. %) with UTS
155 varying from 397.8 to 418.6 MPa and elongation values over 12%. Park et al. [37]
156 reported that the UTS of the Mg-9Al-0.6Zn alloy reached 375 MPa after extrusion at a
157 billet temperature of 523 K (250 °C), extrusion speed of 1 mm/s and a reduction ratio of
158 7.35. Bu et al. [38] developed a new magnesium alloy containing large amounts of
159 alloying elements, including La and Gd (Mg-Al-Zn-RE). The effects of La and Gd on
160 the microstructure and mechanical properties of the extruded alloy were extensively
161 investigated. The results showed that, as a result of La and Gd additions, the $Al_{11}La_3$,
162 Al_8Mn_4Gd and Al_3Gd phases were present in the extruded alloy in addition to the
163 $Mg_{17}Al_{12}$ phase. During extrusion, particle stimulated nucleation (PSN) occurred due to
164 the presence of abundant second-phase particles, leading to the formation of fine,
165 recrystallized grains. The alloy had a UTS of 397 MPa, being higher than that of the
166 traditional magnesium alloy AZ80, owing to a combination of grain refinement

167 strengthening, precipitation strengthening, solid-solution strengthening, dislocation
168 strengthening and subgrain strengthening. Therefore, the alloy was considered to be
169 highly promising for aircraft applications. However, the effects of extrusion process
170 parameters on the microstructure and mechanical properties of the alloy were not
171 investigated. As microstructural changes, such as dynamic recrystallization and
172 precipitation, are largely governed by the local thermomechanical conditions during
173 hot extrusion, it was hypothesized that the as-extruded microstructure and resultant
174 mechanical properties, especially elongation (10%) [38], would be optimized through
175 optimizing the extrusion condition.

176

177 The present work concerned a case study on the extrudability, microstructure evolution
178 during extrusion and the resulting mechanical properties of the newly developed
179 magnesium alloy Mg-Al-Zn-RE. It was intended to serve as an example to show how to
180 determine the extrudability of a new magnesium alloy and understand the effect of
181 extrusion condition on its microstructure and mechanical properties through a
182 combination of experimental research and numerical simulation using the finite
183 element (FE) method. The extrusion experiments were performed by using a
184 tailor-designed die setup. Different combinations of extrusion parameters, namely
185 initial billet temperature, extrusion speed and reduction ratio, were employed. FE
186 simulations of hot extrusion were carried out to predict the extrudate temperature that
187 was hard to measure accurately in real extrusion operation. In addition, the effects of

188 extrusion parameters on the microstructure evolution and mechanical properties of the
189 alloy were investigated through microstructure observation and tensile tests of the
190 extrudate.

191

192 **2. Material, extrusion experiments and numerical simulations**

193 **2.1 Material**

194 The nominal chemical composition of the newly developed Mg-Al-Zn-RE alloy is
195 given in Table 1. The alloy was designed on the basis of AZ81 [38], which is known
196 for having a very narrow range of applicable deformation conditions [39]. The
197 addition of the rare earth elements (i.e., La and Gd) tended to lower its workability
198 further. Hot compression tests indeed showed that this alloy was extraordinarily prone
199 to hot shortness; hot cracking occurred at temperatures higher than 693 K (420 °C).
200 To push the temperature limit upwards, the as-cast alloy was solid-solution-treated at
201 693 K (420 °C) for 24 h, following by water quenching, in order to dissolve
202 second-phase particles, such as Mg₁₇Al₁₂ that has an incipient melting point of 710 K
203 (437 °C) [40]. The solution treatment was also intended to homogenize the as-cast
204 microstructure and improve its extrudability. Cylindrical billets with a diameter of 29
205 mm and lengths of 23 and 15 mm were prepared for extrusion experiments.

206 Table 1. Chemical composition (wt. %) of the Mg-Al-Zn-RE alloy.

Element	Al	Zn	Mn	La	Gd	Mg
---------	----	----	----	----	----	----

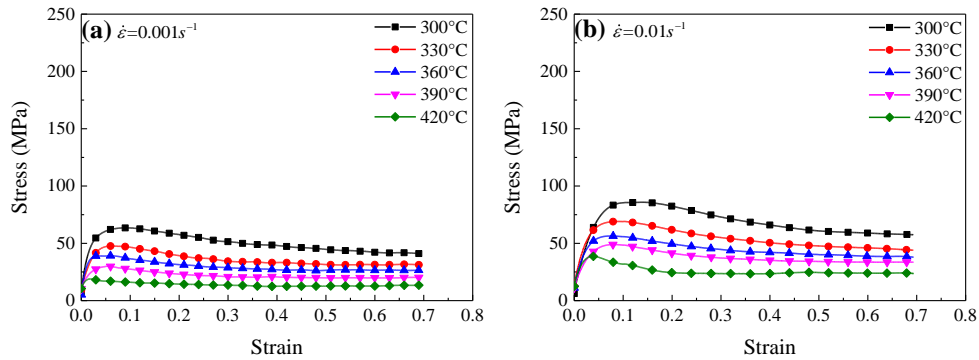
Chemical composition (wt. %)	8.0~8.8	0.3~0.8	0.15~0.3	0.7~1.3	0.3~0.7	Bal.
------------------------------	---------	---------	----------	---------	---------	------

207

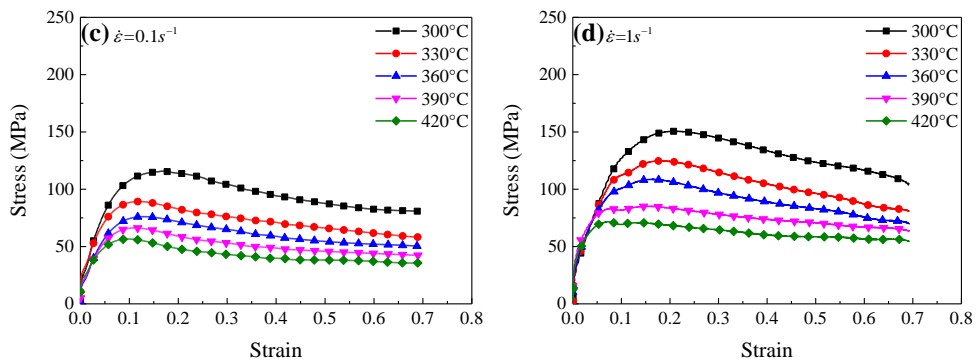
208 2.2 Hot compression tests

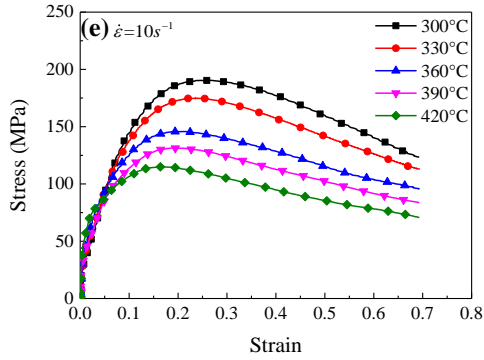
209 A constitutive model of the magnesium alloy is needed for the FE simulations of
 210 extrusion. To determine the constitutive constants, uniaxial compression tests of
 211 cylindrical specimens with sizes of $\phi 8 \times 12$ mm were performed by using a Gleeble
 212 1500 thermomechanical simulator. Test temperatures from 573 K to 693 K (300 °C to
 213 420 °C) and with an interval of 30 K (30 °C) were chosen. Strain rates selected were
 214 0.001, 0.01, 0.1, 1 and 10 s⁻¹. The flow stress-strain curves obtained at different
 215 temperatures and strain rates are shown in Fig. 1. The hyperbolic sine-type equation
 216 (Eq. 1), proposed by Sellars and McTegart [41], was adopted to describe the
 217 deformation behavior of the material.

218



219





220

221 Fig. 1. Flow stress-strain curves of the magnesium alloy at temperatures from 573 K to
 222 693 K (300 °C to 420 °C) and strain rates (a) 0.001 s⁻¹, (b) 0.01 s⁻¹, (c) 0.1 s⁻¹, (d) 1 s⁻¹
 223 and (e) 10 s⁻¹.

224
$$\dot{\epsilon} = A[\sinh(\alpha\sigma)]^n \exp\left(\frac{-Q}{RT}\right) \quad (1)$$

225 where, A , α and n are material constants, Q is the activation energy for hot

226 deformation, and R is the gas constant. The constitutive constants obtained were used

227 as material constants in the model for the FE simulations of extrusion (Table 2).

228

229 Table 2. Constitutive constants of the magnesium alloy (Mg-Al-Zn-RE).

Constitutive constant	A	α	n	Q (kJ/mol)
Value	2.3188e+10	1.721e-2	4.5164	141.329

230

231 2.3 Extrusion tooling setup

232 The tooling setup, specially designed for this research, consisted of a structural

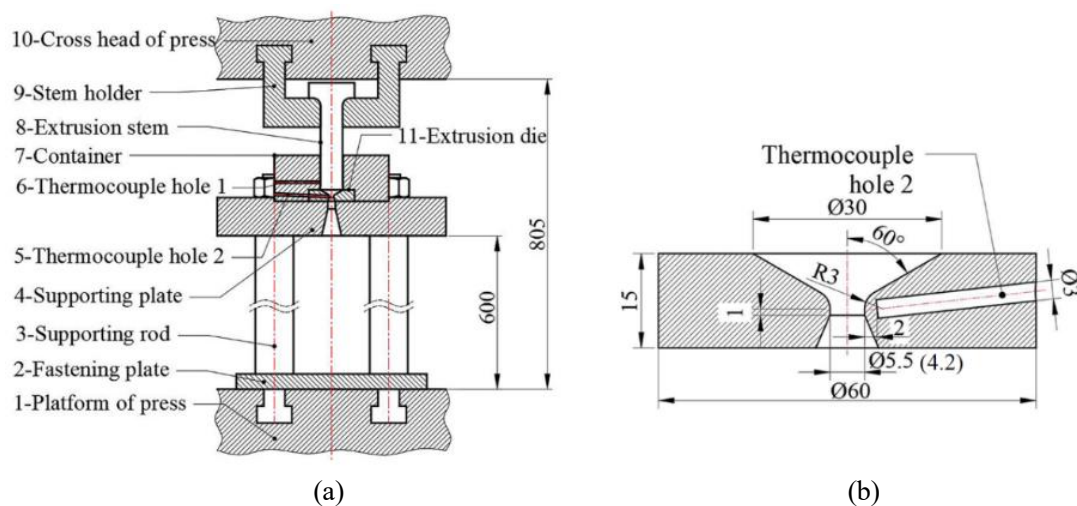
233 supporting framework, a heating system, a die with a round opening, a container, a

234 stem and a stem holder (Fig. 2). The supporting framework included a fastening plate,

235 supporting rods and a supporting plate, which were used to fix the die setup on the

236 platform of a press driven by a hydraulic system. The stem holder was connected to

237 the crosshead of the hydraulic press. Four resistance-heating elements with a total
 238 power of 2000 W were employed to heat the container, extrusion die and billet.
 239 Heating was controlled by a PID (Proportion Integration Differentiation) controller
 240 based on the feedback temperature measured by Thermocouple 1. Thermocouple 2
 241 was inserted into the die to measure the temperature near the die orifice during
 242 extrusion. The measuring point was 2 mm away from the die bearing (Fig. 2b).
 243
 244 Two extrusion dies with orifice diameters of 5.5 and 4.2 mm were employed for
 245 extrusion at reduction ratios of 29.8 and 51.0, respectively, while the diameter of the
 246 container liner stayed unchanged (30 mm). For each die, the inlet angle was 60° and
 247 the length of straight die bearing was 1 mm.



248
 249

250 Fig. 2. Tooling set-up to extrude rods: (a) schematic and (b) dimensions of one of the extrusion dies.

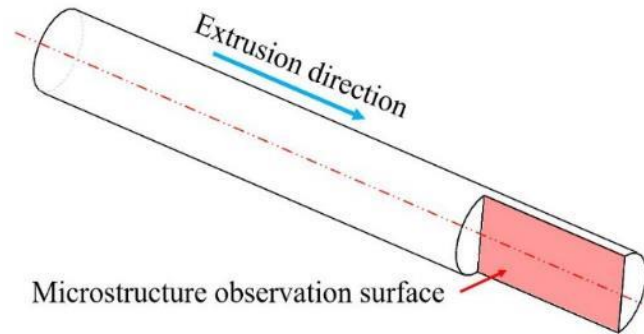
251 **2.4 Extrusion experiments**

252 Extrusion experiments were performed by using the tooling setup mounted on a
253 hydraulic press with a force capacity of 2 MN. Before extrusion, the billet was heated
254 to a preset temperature at a rate of 8 K/min (8 °C/min) and soaked for 15 min. The
255 container and die were heated to the same temperature as the billet. During extrusion,
256 the temperature near the die orifice was measured by Thermocouple 2. After extrusion,
257 the extruded rod was cut off from the discard and air-cooled. Initial billet temperature,
258 extrusion speed and reduction ratio were taken as the main process variables. Initial
259 billet temperature was set at 523, 573, 623, 673 and 713 K (250, 300, 350, 400 and
260 440 °C). Stem speed increased from 0.48 mm/s to 8.24 mm/s. Reduction ratios were
261 29.8 and 51.0, as mentioned in Subsection 2.3.

262 **2.5 Microstructure observation**

263 Samples were cut from the extruded rods along the longitudinal extrusion direction
264 (Fig. 3). The exposed surfaces were ground and mechanically polished. An etchant
265 composed of 5 g picric acid, 10 ml acetic acid, 10 ml deionized water and 100 ml
266 absolute ethyl alcohol was used to etch the samples. The microstructures of the
267 samples were observed using an optical microscope (Zeiss Axio Scope.A1) and a
268 scanning electron microscope (SEM, FEI Quanta 200 FEG) equipped with an energy
269 dispersive x-ray spectroscope (EDS). The grain sizes of the extrudate were
270 determined by using the linear intercept method. The sizes and volume fractions of

271 second-phase particles were measured by using the commercial software Image-Pro
272 Plus on the basis of SEM micrographs.



273

274 Fig. 3. Schematic of the longitudinal section of an extruded rod for microstructure observation.

275 2.6 Tensile tests

276 Tensile specimens were prepared by machining from the extruded rods. They had a
277 total length of 90 mm, a gauge length of 25 mm and a gauge diameter of 4 mm,
278 conforming to the standard GB/T 228.1-2010. Tensile tests were conducted using a
279 universal material testing machine (AG-X, Shimadzu) at a crosshead speed of 1
280 mm/min. Tensile force was applied in the direction being the same as the extrusion
281 direction. The test of the specimen processed under each condition was repeated at
282 least twice to ensure the reproducibility of the data.

283

284 2.7 Finite element simulations

285 FE simulations were performed to predict the temperature of the extrudate at the die
286 orifice, as affected by the extrusion variables. An axisymmetric FE model (Fig. 4) was

287 built by using the commercial software package DEFORM. The billet, extrusion die,
 288 stem and container were all meshed to be composed of quadrilateral elements. The
 289 billet was defined as a thermo-rigid-plastic material, and the thermomechanical effect
 290 occurring during extrusion was taken into account. The extrusion tools were
 291 considered to be rigid objects and heat transfer was allowed. The constitutive equation
 292 (Eq. 1) was applied in the FE simulations. The initial temperatures of the container
 293 and die were set to be the same as those used in the extrusion experiments, while the
 294 stem was set at an initial temperature of 293 K (20 °C). Heat exchanges between the
 295 billet, extrusion tooling and surrounding environment were taken into consideration. A
 296 shear friction model was adopted at the interfaces between the billet and extrusion
 297 tooling and the friction coefficient was set at 1.0 [42]. The physical properties of the
 298 magnesium alloy and tooling material (H13 tool steel) are listed in Table 3 [43].

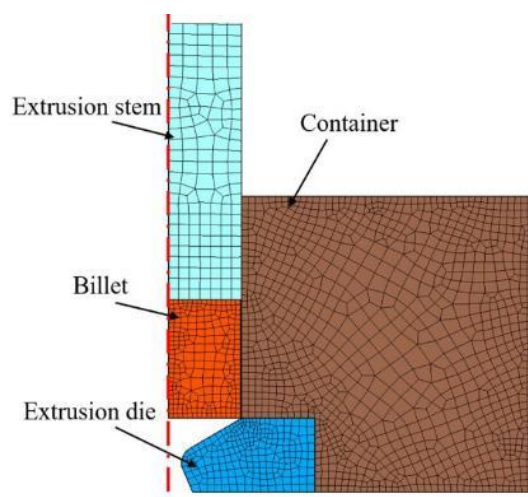


Fig. 4. Axisymmetric FE model to simulate the extrusion process to produce rods.

Table 3. Physical properties of the billet and extrusion tooling.

Physical property	Magnesium alloy	H13 tool steel
-------------------	-----------------	----------------

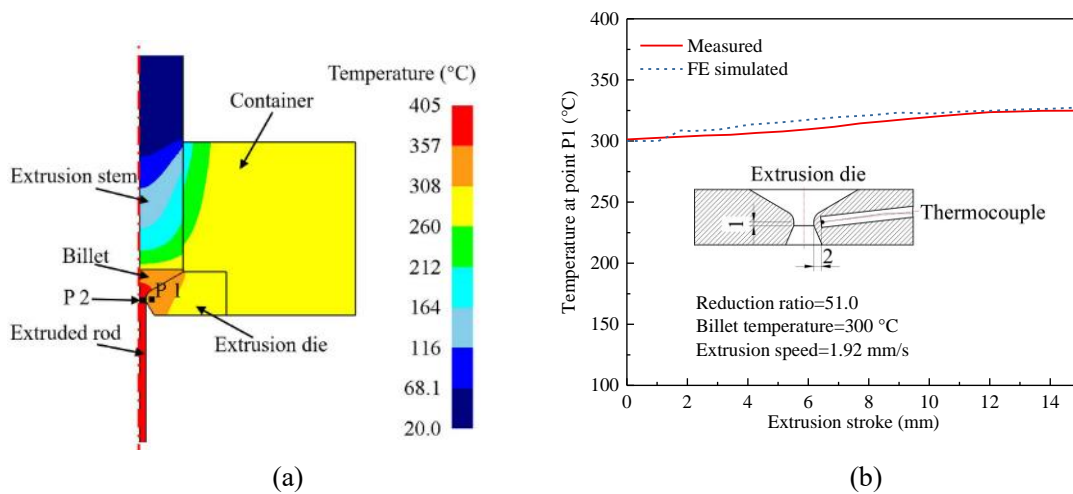
Thermal conductivity (W/(m °C))	96	28.4
Heat capacity (N/(mm ² °C))	2.097 at 600 K (327°C)	5.6
	2.275 at 800 K (527°C)	
Heat transfer coefficient between tooling and workpiece (N/(°C s mm ²))	11	11
Heat transfer coefficient between tooling/workpiece and air (N/(°C s mm ²))	0.02	0.02
Emissivity	0.7	0.7

302 **3. Results and discussion**

303 **3.1 Extrudate temperature**

304 The extrudate temperature at the die exit, the most important process parameter that
305 strongly influences the surface quality and microstructure of the extrudate, depends on
306 the initial billet temperature, extrusion speed and reduction ratio. It is however
307 difficult to measure directly and accurately. To verify the extrudate temperature
308 predicted from FE simulations, comparisons with the temperatures near the die
309 bearing, measured by inserted Thermocouple 2, were made. Fig. 5a shows an example
310 of the predicted temperature distribution inside the extruded billet, rod, and extrusion
311 tooling, when the initial billet temperature was 573 K (300 °C), reduction ratio 51.0
312 and stem speed 1.92 mm/s. The temperature predicted at point P1 inside the die
313 reached a peak value of 600 K (327 °C) at a stem displacement of 15 mm. It was very
314 close to the value of 598 K (325 °C) measured by Thermocouple 2. In addition, the
315 calculated and measured temperature evolutions at point P1 during extrusion were

316 compared. The results (Fig. 5b) showed that the simulated temperatures were in
 317 agreement with the experimentally measured values. The differences between
 318 simulated and measured temperatures were negligible. It indicated that the present FE
 319 model of extrusion was reliable in temperature calculation. Based on this fact, we
 320 considered the calculated temperature at point P2 to be the exact temperature of the
 321 extrudate surface. In addition, a large difference in temperature between the extrudate
 322 surface (678 K, i.e., 405 °C at point P2) and measuring point (600 K, i.e., 327 °C at
 323 point P1) was found, even though there was a distance of only 2 mm between these
 324 two points. It confirmed that the measured die temperature could not be used as the
 325 temperature of the extrudate directly.



326
 327

328 Fig. 5. Predicted temperature distribution inside the billet, extrudate and extrusion tooling (a) and
 329 comparison between the measured and predicted temperatures at P1 along with stem displacement
 330 (b).

331

332 Fig. 6 shows the FE simulated temperature evolutions at point P2 under different
333 extrusion conditions. At the initial stage of extrusion, the temperature at point P2 rose
334 significantly, which was attributed to heat generation from both plastic deformation
335 and severe friction between the billet and tooling. The temperature rise due to
336 deformation heating can be described by using Eq. 2, where η is the adiabatic factor
337 with a value between 0.9 and 0.95, and ρ is the specific density and C_p is the specific
338 heat [44].

$$339 \quad \Delta T = \frac{\eta \int \sigma d\varepsilon}{\rho C_p} \quad (2)$$

340

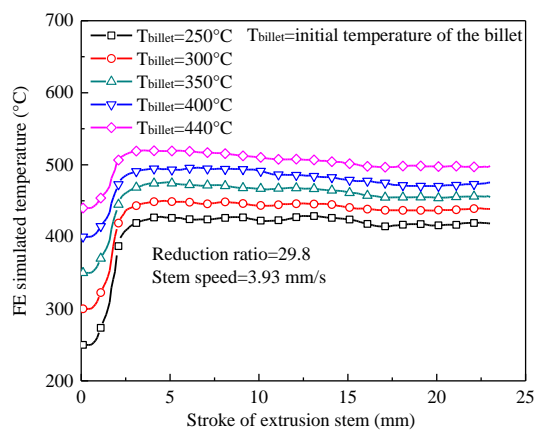
341 Eq. 3 gives the shear-type friction model employed during the simulations, where τ is
342 the shear stress, and m is the friction factor [45]. The friction factor was set to be 1,
343 considering the severe friction between the tooling and billet [42]. The frictional
344 heating contributed to temperature rise during the extrusion process. In the meantime,
345 heat was transferred between the billet and tooling and dissipated into the atmosphere.
346 With rising extrudate temperature, more heat was transferred from the extrudate to the
347 tooling. Heat generation and dissipation to the die competed with each other, and then
348 the extrudate temperature reached a steady state.

$$349 \quad \tau = \frac{m\sigma}{\sqrt{3}} \quad (3)$$

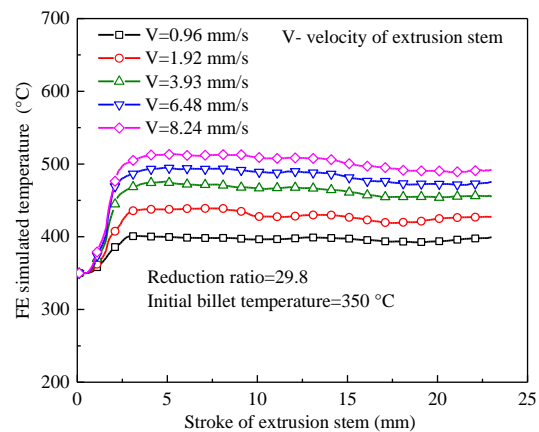
350 Fig. 7 shows the simulated temperatures at point P2, when two different friction factor
351 values of 0 and 1 were applied. The same reduction ratio of 29.8, extrusion speed of

352 3.93 mm/s and initial billet temperature 523 K (250 °C) were employed in these
 353 simulations. When the fraction factor values were 0 and 1, the temperature increments
 354 of extrudate were 124 K and 179 K (124 °C and 179 °C), respectively. The result was
 355 consistent with the above statement that the temperature increment during extrusion
 356 was partially attributed to the heat generation from severe friction between the billet
 357 and tooling.

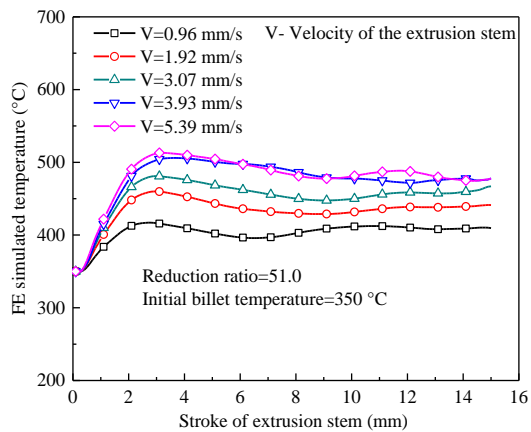
358
 359
 360
 361



(a)



(b)



(c)

362

363

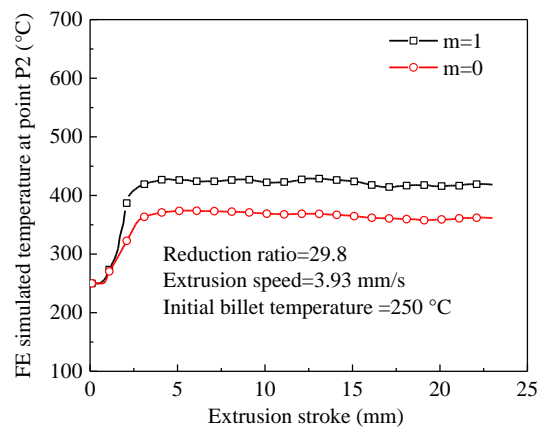
364

365

366 Fig. 6. FE simulated temperature evolutions at point P2 during extrusion: (a) at a reduction ratio of
 367 29.8, stem speed of 3.93 mm/s and different initial billet temperatures, (b) at a reduction ratio of
 368 29.8, initial billet temperature of 623 K (350 °C) and different stem speeds, and (c) at a reduction
 369 ratio of 51.0, initial billet temperature of 623 K (350 °C) and different stem speeds.

370

371



372

373

Fig. 7. Simulated temperatures at point P2 with friction factor values of 0 and 1.

374

375 When reduction ratio was 29.8 and stem speed 3.93 mm/s, the maximum extrudate
 376 temperatures reached 702, 723, 749 769 and 793 K (429, 450, 476, 496 and 520 °C)
 377 during extrusion at initial temperatures of 523, 573, 623, 673 and 713 K (250, 300,
 378 350, 400 and 440 °C), respectively (Fig. 6a), meaning temperature increments of 179,
 379 150, 126, 96 and 80 K (179, 150, 126, 96 and 80 °C), respectively. As the initial billet
 380 temperature increased, the temperature increment during extrusion decreased. This
 381 can be explained by the fact that the lower the initial billet temperature, the more heat
 382 generation from the higher flow stress of the magnesium alloy.

383

384 Fig. 6b shows the temperature evolutions at a reduction ratio of 29.8, initial billet
385 temperature of 623 K (350 °C) and stem speeds of 0.96, 1.92, 3.93, 6.48 and 8.24
386 mm/s. The maximum temperature increments were 61, 89, 126, 145 and 154 K (61,
387 89, 126, 145 and 154 °C), respectively. With increasing extrusion speed, the
388 maximum temperature of the extrudate grew. There are two factors that lead to the
389 increases in extrudate temperature. On the one hand, the enhanced flow stress of the
390 billet material at a higher extrusion speed leads to more heat generation than that at a
391 lower extrusion speed. On the other hand, heat generation at a higher extrusion speed
392 is less dissipated to the die.

393

394 When reduction ratio increased to 51.0 and the initial billet temperature remained
395 unchanged (623 K, i.e., 350 °C), the maximum temperature increments were 67, 110,
396 131, 206 and 213 K (67, 110, 131, 206 and 213 °C), at stem speeds of 0.96, 1.92, 3.07,
397 3.93 and 5.39 mm/s, respectively (Fig. 6c). Comparison between the extrudate
398 temperatures at these two reduction ratios (Fig. 6b and c) showed that a larger
399 temperature increment appeared at a higher reduction ratio, but at the same initial
400 billet temperature and extrusion speed. It can be explained by the fact that a higher
401 strain rate at a larger reduction ratio contributes to the temperature increase of the
402 extrudate.

403

404 3.2 Surface quality

405 The surface quality of an extruded magnesium alloy rod is negatively influenced by
406 the defect of hot shortness. In general, the tendency for hot shortness to occur
407 increases with increasing initial billet temperature, reduction ratio and extrusion speed.
408 It is caused by an excessively high temperature due to heat generation inside the
409 magnesium alloy undergoing large plastic deformation during extrusion. Figs. 8-10
410 show three groups of extruded magnesium alloy rods, which are arranged in a
411 convenient way to demonstrate the influences of the initial billet temperature,
412 extrusion speed and reduction ratio on the surface quality of the extruded rods.

413

414 Fig. 8 shows the magnesium alloy rods extruded at a reduction ratio of 29.8, stem
415 speed of 3.93 mm/s and different initial billet temperatures. Defect-free surfaces of
416 the extruded rods were obtained, when the initial billet temperatures were lower than
417 673 K (400 °C) (Fig. 8a-c). When the initial billet temperature increased to 673 K
418 (400 °C), however, hot shortness occurred on the surface of the extruded rod (Fig. 8d).
419 With a further increase in initial billet temperature to 713 K (440 °C), large and deep
420 cracks on the surface of the extruded rod became visible to the naked eye (Fig. 8e).
421 For the rods extruded under these conditions, FE simulation predicted the maximum
422 extrudate temperatures T_e of 769 K and 793 K (496 °C and 520 °C). It could be
423 inferred that the critical temperature for hot shortness to occur lay from 749 K to 769
424 K (476 °C to 496 °C). It was thus the initial billet temperature that influenced the

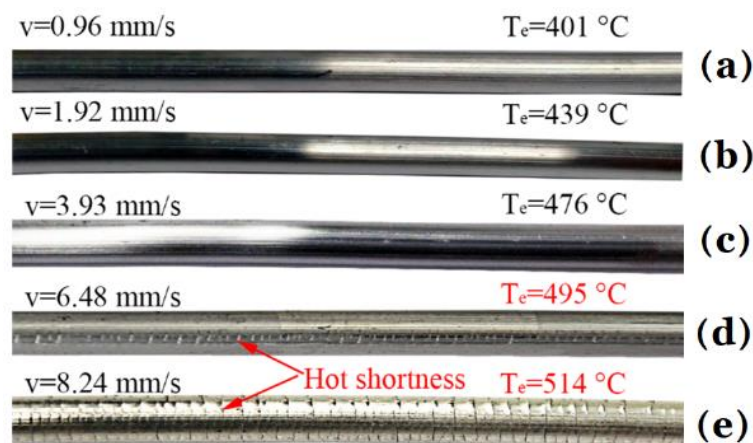
425 surface quality of the extrudate [46, 47]. At the die bearing, tensile stresses due to
 426 severe friction exceeded the tensile strength of the material at the surface and
 427 consequently tearing occurred (Fig. 8d). If the heat generated from friction and hot
 428 deformation led to further temperature increases at the die bearing to the incipient
 429 melting point, localized melting took place, which would cause severe cracking on the
 430 surface (Fig. 8e).



431
 432 Fig. 8. Magnesium alloy rods extruded at a reduction ratio of 29.8, stem speed of 3.93 mm/s and
 433 different billet temperatures. T_e is the maximum extrudate temperature. (a) $T=523$ K (250 °C) and
 434 $T_e=702$ K (429 °C); (b) $T=573$ K (300 °C) and $T_e=723$ K (450 °C); (c) $T=623$ K (350 °C) and
 435 $T_e=749$ K (476 °C); (d) $T=673$ K (400 °C) and $T_e=769$ K (496 °C); (e) $T=713$ K (440 °C) and
 436 $T_e=793$ K (520 °C).

437 Extrusion speed is another factor influencing the surface quality of the extrudate,
 438 which embodies heat generation and dissipation during extrusion. It is obvious that
 439 heat generation increases with increasing extrusion speed, because a higher strain rate
 440 corresponds to more dynamic plastic deformation, and less heat is dissipated to the

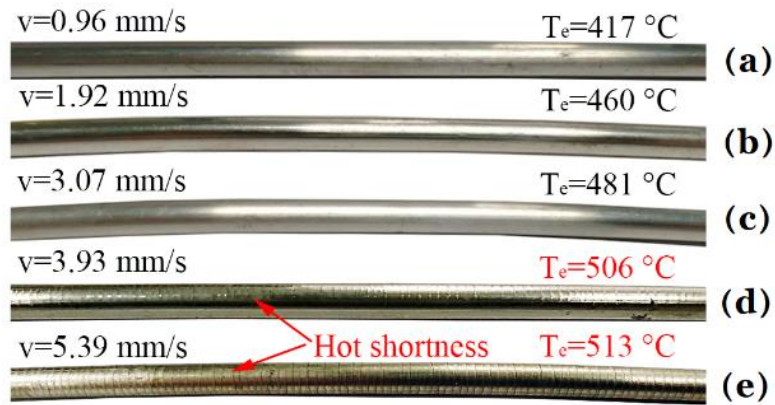
441 surrounding as a result of shortened process time, as shown in Fig. 6b. It is the raised
 442 extrudate temperature that limits the applicable extrusion speed. In the present
 443 research, at the same initial billet temperature of 623 K (350 °C) and reduction ratio
 444 of 29.8, the rods extruded at different stem speeds had different surface features (Fig.
 445 9). When stem speeds were lower than 3.93 mm/s, the extruded magnesium alloy rods
 446 had smooth surface finish (Fig. 9a-c). When stem speed increased to 6.48 mm/s,
 447 however, minor cracks appeared on the surface of the extruded rod (Fig. 9d). Severe
 448 hot shortness occurred at the stem speed of 8.24 mm/s (Fig. 9e). FE simulations
 449 indicated the extrudate surface temperatures of 749, 768 and 787 K (476, 495 and
 450 514 °C), at stem speeds of 3.93, 6.48 and 8.24 mm/s, respectively (Fig. 6b). In
 451 combination with the results shown earlier in Fig. 8d, the critical temperature for hot
 452 shortness to occur would be in the range of 749 K and 768 K (476 °C and 495 °C).



453
 454 Fig. 9. Magnesium alloy rods extruded at a reduction ratio of 29.8, initial billet temperature of 623
 455 K (350 °C) and different stem speeds. (a) $v = 0.96$ mm/s and $T_e = 674$ K (401 °C); (b) $v = 1.92$ mm/s

456 and $T_e=712$ K (439 °C); (c) $v=3.93$ mm/s and $T_e=749$ K (476 °C); (d) $v=6.48$ mm/s and $T_e=768$ K
457 (495 °C); (e) $v=8.24$ mm/s and $T_e=787$ K (514 °C). T_e is the maximum extrudate temperature.

458 As mentioned earlier, heat generated from the plastic deformation of the billet
459 material leads to the temperature rise of the extrudate. Reduction ratio is a process
460 parameter that is directly related to the amount of plastic deformation. The extrusion
461 experiments performed at a higher reduction ratio of 51.0 clearly depicted the effect
462 of reduction ratio on extrudate surface quality (compare Fig. 10 and Fig. 9). When
463 reduction ratio was 51.0, initial billet temperature 623 K (350 °C) and stem speed
464 3.93 mm/s, the maximum extrudate temperature reached 779 K (506 °C) and hot
465 shortness occurred. At the lower reduction ratio of 29.8, however, the extrudate
466 exhibited sound surface (Fig. 9c) and under this extrusion condition the maximum
467 extrudate temperature was only 749 K (476 °C). It clearly indicated that the high
468 reduction ratio increased the tendency of hot shortness. Fig. 10c shows the good
469 surface of the extrudate at a stem speed of 3.07 mm/s and under this extrusion
470 condition the extrudate temperature was 754 K (481 °C). By combining the results
471 shown in Figs. 8, 9 and 10, one may infer the critical temperature for hot shortness to
472 occur to be in the range of 754 K and 768 K (481 °C to 495 °C). The extrudate
473 temperature of 754 K (481 °C) can be taken as a conservative critical temperature to
474 avoid hot shortness.



475

476 Fig. 10. Magnesium alloy rods extruded at a reduction ratio of 51.0, initial billet temperature of

477 623 K (350 °C) and different stem speeds. (a) $v=0.96$ mm/s and $T_e=987$ K (417 °C); (b) $v=1.92$

478 mm/s and $T_e=733$ K (460 °C); (c) $v=3.07$ mm/s and $T_e=754$ K (481 °C); (d) $v=3.93$ mm/s and

479 $T_e=779$ K (506 °C); (e) $v=5.39$ mm/s and $T_e=786$ K (513 °C). T_e is the maximum extrudate

480 temperature.

481

482

483 3.3 Microstructures

484 Fig. 11 shows the microstructures of the as-cast and the as-solid-solution-treated

485 Mg-Al-Zn-RE alloy. The as-cast alloy had a dendritic magnesium matrix and

486 interdendritic second-phase particles (Fig. 11a). Morphology and composition

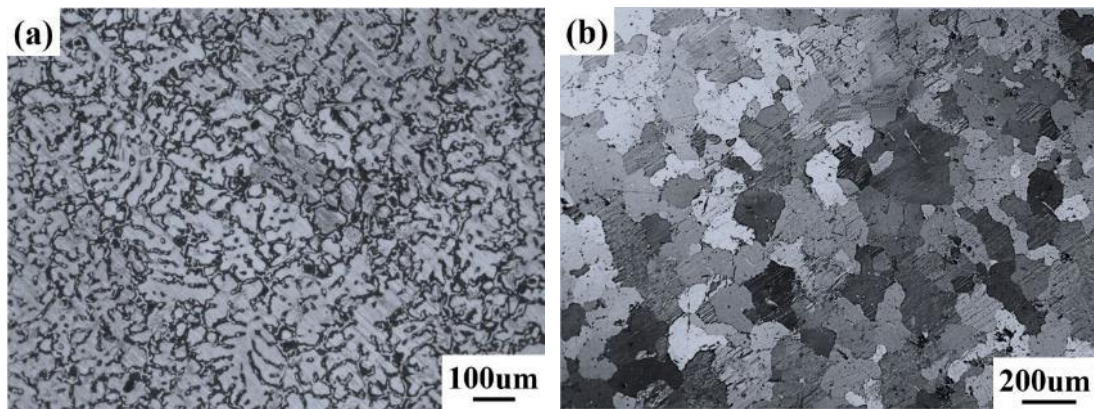
487 analyses indicated the presence of four kinds of second-phase particles in the as-cast

488 alloy, namely reticulate phase $Mg_{17}Al_{12}$, needle-like or lamellar phase $Al_{11}La_3$, and

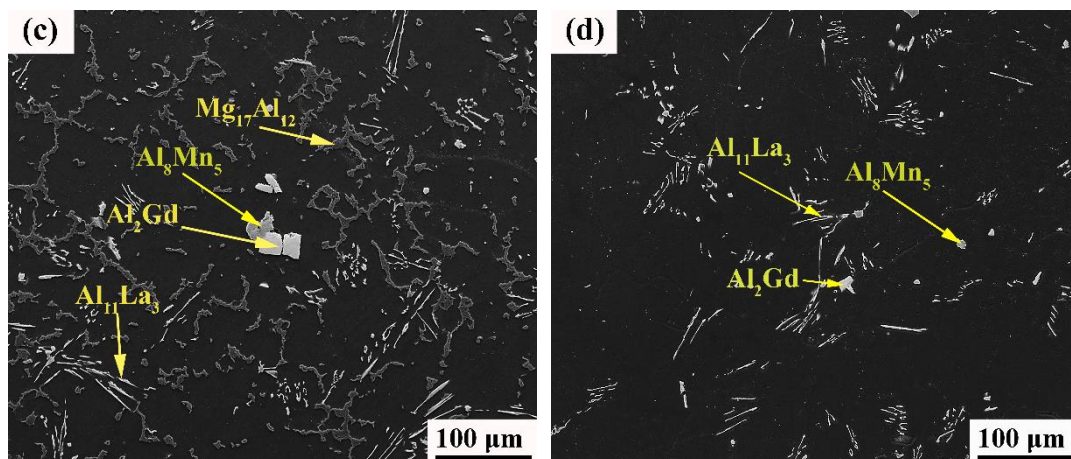
489 block-shaped phases Al_8Mn_5 and Al_2Gd (Figs. 11c, e-h and Table 4). $Mg_{17}Al_{12}$ and

490 Al_8Mn_5 were the common intermetallic compounds in commercial Mg-Al-Zn alloys

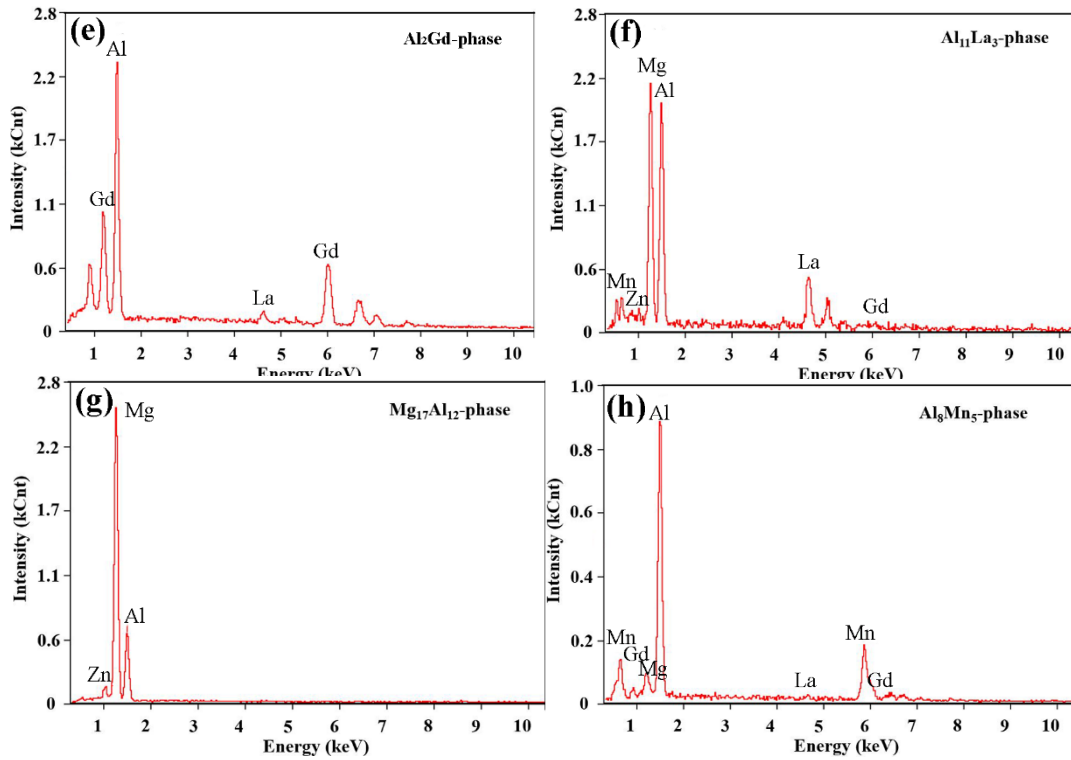
491 with a high Al content [48, 49]. $\text{Al}_{11}\text{La}_3$ and Al_2Gd were the compounds whose
492 formation was due to the addition of rare earth elements of La and Ga [38, 50-51] to
493 the Mg-Al-Zn base alloy. The volume fraction of second-phase particles in the SEM
494 micrograph of the as-cast alloy was 7.3% (Fig. 11c). After the solid-solution treatment
495 at 693 K (420 °C) for 24 h, the $\text{Mg}_{17}\text{Al}_{12}$ phase with a melting point of 701 K (437 °C)
496 [40] disappeared due to its dissolution into the Mg matrix. The volume fraction of
497 second-phase particles decreased significantly to 2.1% (Fig. 11d). During the heat
498 treatment, the as-cast dendritic structure changed to an equiaxed grain structure; the
499 mean grain size determined by using the linear intercept method [52] was $165 (\pm 5)$
500 μm (Fig. 11b).



501



502



503

504

505 Fig. 11. Microstructures of the Mg-Al-Zn-RE alloy: (a) dendritic structure of the as-cast alloy; (b)
 506 equiaxed grain structure of the solid-solution-treated alloy; (c) SEM micrograph of the as-cast
 507 alloy; (d) SEM micrograph of the solid-solution treated alloy; (e-h) EDS element maps of Al_2Gd ,
 508 $\text{Al}_{11}\text{La}_3$, $\text{Mg}_{17}\text{Al}_{12}$ and Al_8Mn_5 phases.

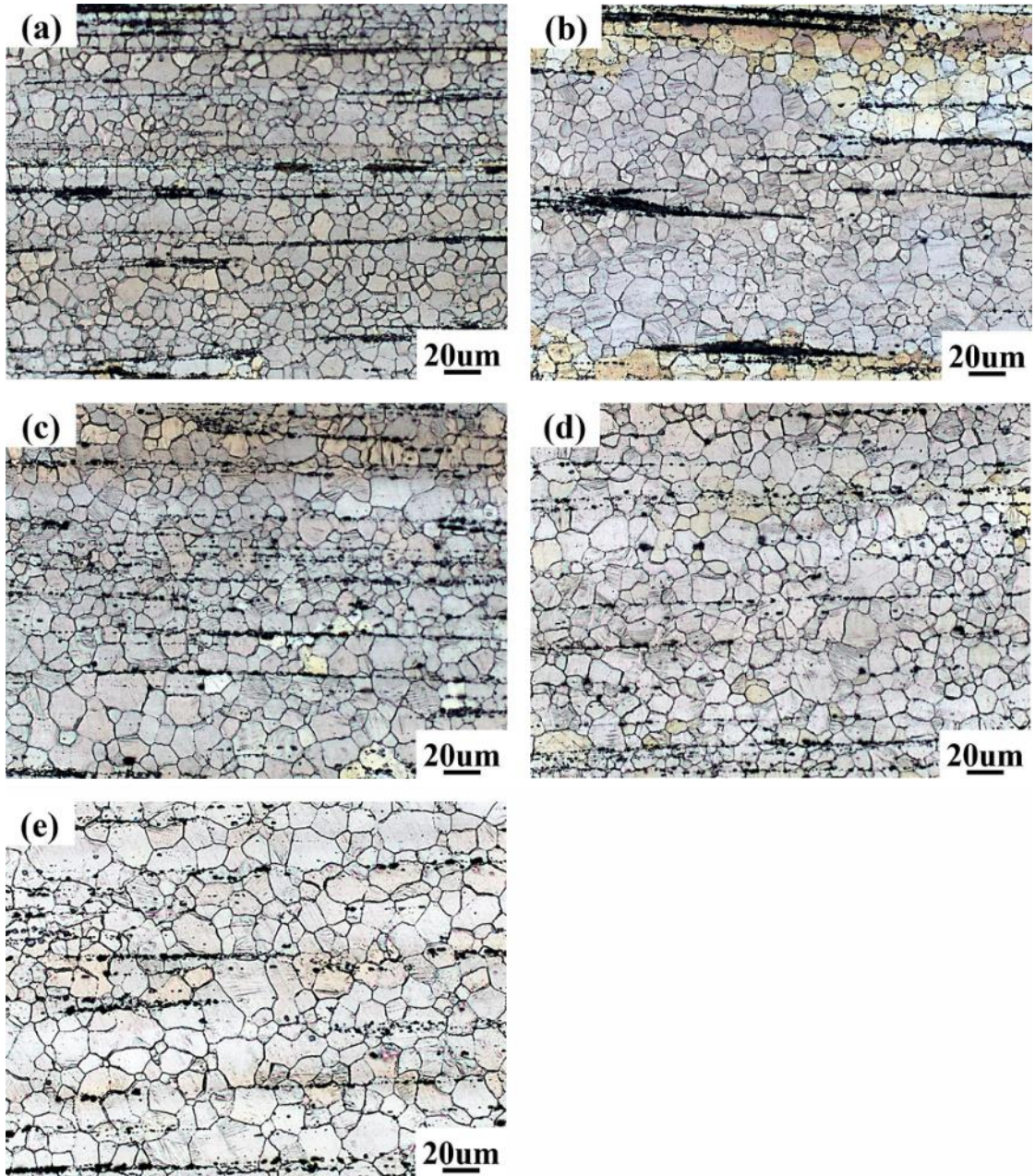
509

Table 4. EDS analysis of second-phase particles in the as-cast alloy.

Phases	Al_2Gd	$\text{Al}_{11}\text{La}_3$	$\text{Mg}_{17}\text{Al}_{12}$	Al_8Mn_5
Mg (at. %)		49.84	69.06	1.99
Al (at. %)	68.08	37.25	29.24	64.92
Zn (at. %)		0.78	1.70	
Mn (at. %)		0.41		25.70
La (at. %)	2.90	9.58		
Gd (at. %)	29.03	2.14		6.62

510

511 The optical microstructures of the magnesium alloy rods extruded at temperatures of
512 523-713 K (250-440 °C), a reduction ratio of 29.8 and stem speed of 3.93 mm/s are
513 shown in Fig. 12. Apparently, dynamic recrystallization (DRX) occurred during
514 extrusion under these conditions, and the mean grain sizes of the extruded magnesium
515 alloy rods reduced significantly from the mean value of the as-solid-solution-treated
516 alloy. The mean grain sizes of the rods extruded at 523, 573, 623, 673, 673 and 713 K
517 (250, 300, 350, 400 and 440 °C) were 8.0 (± 0.3), 8.5 (± 0.5), 9.5 (± 0.3), 10.9 (\pm
518 0.3) and 12.4 (± 0.4) μm , respectively, showing an increasing trend with rising initial
519 billet temperature.



520

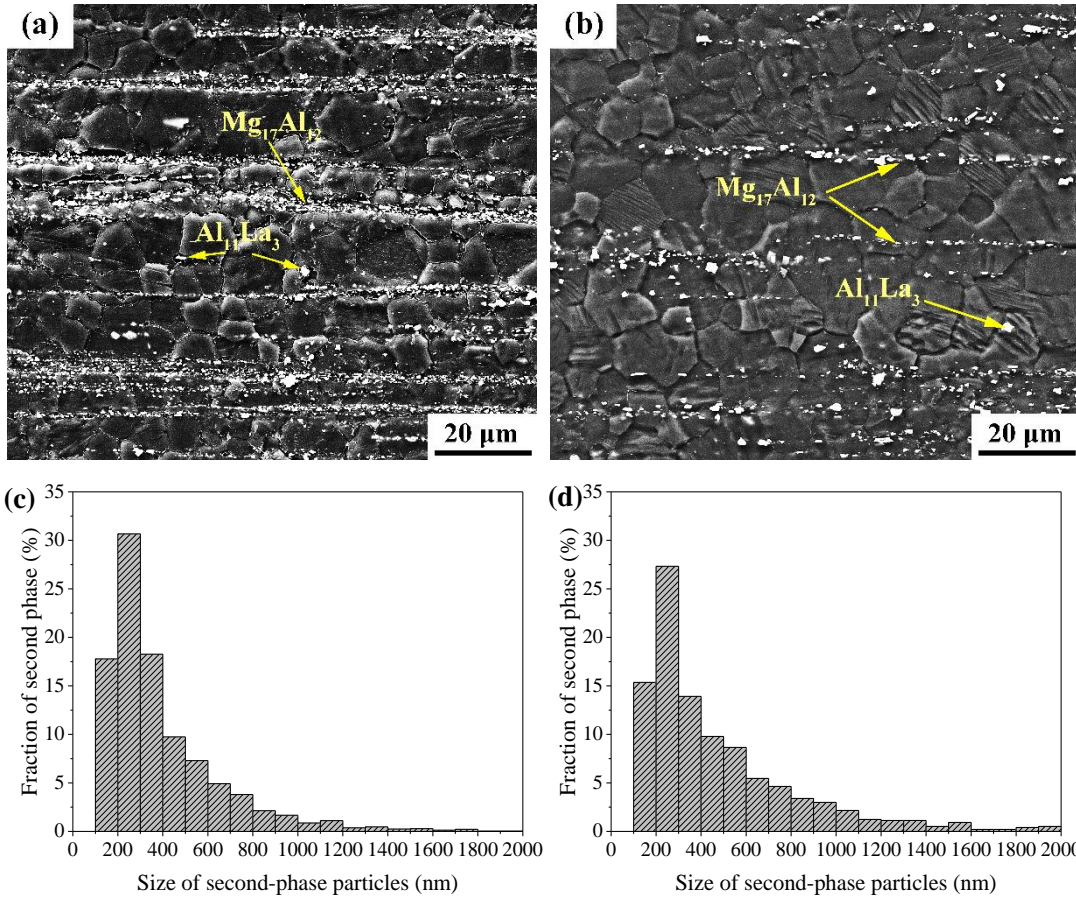
521 Fig. 12. Optical micrographs of the magnesium alloy rods extruded at a reduction ratio of 29.8,
 522 stem speed of 3.93 mm/s and initial billet temperatures of (a) 523, (b) 573, (c) 623, (d) 673 and (e)
 523 713 K [(a) 250, (b) 300, (c) 350, (d) 400 and (e) 440 °C].

524

525 The second phase $Mg_{17}Al_{12}$ reappeared due to dynamic precipitation from the
 526 supersaturated magnesium solid solution during extrusion and became distributed

527 along the extrusion direction (Fig. 13). The needle-like or lamellar phase $Al_{11}La_3$ in
528 the as-solid-solution-treated alloy was broken up and became block-shaped particles
529 during extrusion. The sizes of second-phase particles increased, but their volume
530 fraction decreased with increasing initial billet temperature. At the initial billet
531 temperature of 523 K (250 °C), the maximum temperature of the extrudate reached
532 702 K (429 °C) and a lot of fine second-phase particles with sizes smaller than 1,000
533 nm were distributed on recrystallized grain boundaries (Figs. 13a and c). The mean
534 size of second-phase particles was 397 nm, and the volume fraction was 5.4%. At an
535 increased initial billet temperature of 623 K (350 °C), the maximum temperature of
536 the extrudate increased to 749 K (476 °C), the volume fraction of second-phase
537 particles with sizes of 1,000 nm and larger increased and the mean size of
538 second-phase particles increased to 492 nm. However, the overall volume fraction of
539 second-phase particles decreased to 2.8% (Figs. 13b and d) as a result of higher
540 solubility of the alloying elements in the magnesium matrix at a higher temperature.
541 This phenomenon also was found in other magnesium alloys with high Al contents
542 during extrusion [53, 54]. In addition to the dissolution of small particles, the alloying
543 elements diffused and became accumulated at existing, larger particles, which resulted
544 in particle growth.

545



546

547

548

549 Fig. 13. SEM micrographs and distributions of the sizes of second-phases particles in the rods

550 extruded at a reduction ratio of 29.8, stem speed of 3.93 mm/s and initial billet temperatures of (a)

551 (c) 523 K (250 °C) and (b) (d) 623 K (350 °C).

552

553 Fig. 14 shows the optical micrographs of the magnesium alloy rods extruded at a

554 billet temperature of 623 K (350 °C), reduction ratio of 29.8 and different stem speeds.

555 With increases in stem speed from 0.96 to 1.92, 3.93, 6.48 and 8.24 mm/s, the mean

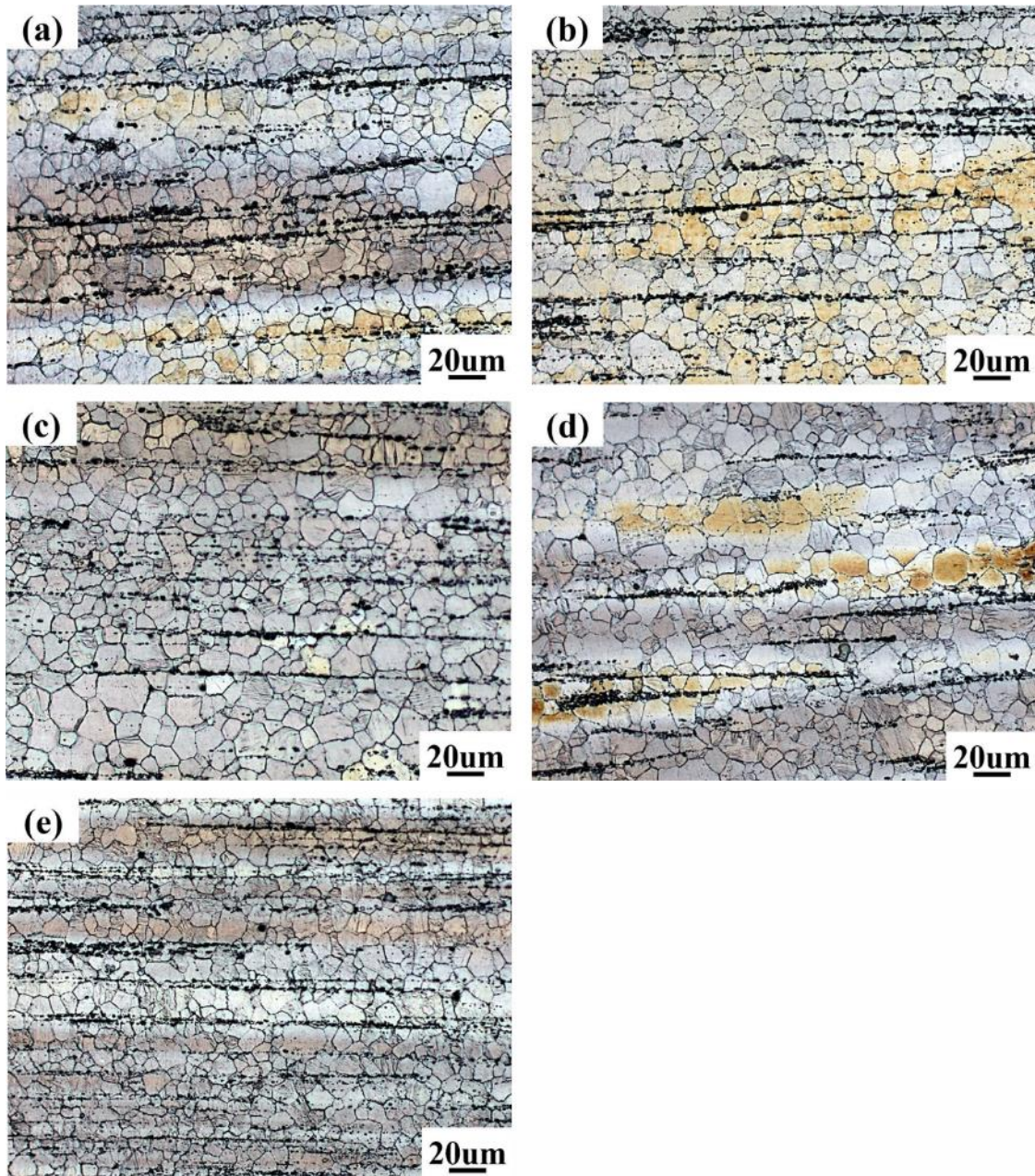
556 grain sizes of the extruded magnesium rods rose marginally from 8.6 (± 0.5) to 8.9

557 (± 0.4), 9.5 (± 0.3), 9.8 (± 0.6) and 10.1 (0.5) μm, respectively. On the one hand, the

558 extrudate temperature increased with increasing extrusion speed; the maximum

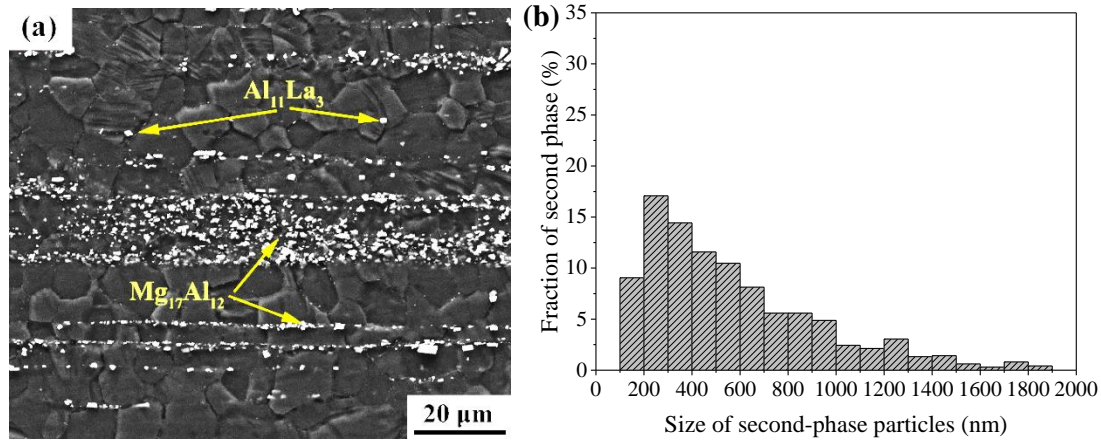
559 extrudate temperature reached 674-787 K (401-514 °C) when stem speed increased
560 from 0.96 to 8.24 mm/s (Fig. 6b). A high extrudate temperature would normally
561 promote the growth of DRX grains. But on the other hand, the equivalent strain rate
562 increased with increasing extrusion speed and a high strain rate would contribute to
563 grain refinement during the hot deformation of magnesium alloys [55]. In addition,
564 with increasing extrusion speed, the sizes and volume fraction of second-phase
565 particles changed, which would affect grain sizes. Fig. 15 presents an SEM
566 micrograph and a size distribution of second-phase particles in the magnesium alloy
567 rod extruded at a reduction ratio of 29.8, initial billet temperature of 623 K (350 °C)
568 and stem speed of 0.96 mm/s. The data could be compared with those obtained from
569 the magnesium rod extruded at a higher stem speed of 3.93 mm/s, but at the same
570 reduction ratio and initial billet temperature (Figs. 13b and d). With an increase in
571 stem speed from 0.96 to 3.93 mm/s, the volume fraction of second-phase particles
572 decreased from 3.6% to 2.8%, and the mean size decreased from 577 to 492 nm. The
573 maximum extrudate temperature at stem speeds of 0.96 mm/s and 3.93 mm/s rose to
574 674 K to 745 K (401 °C and 472 °C), respectively. Clearly, it was the lower extrudate
575 temperature at a lower extrusion speed that resulted in more and larger dynamically
576 precipitated second-phase particles, as a result of longer time given for particle
577 precipitation and growth. Comparison between Fig. 13d and Fig. 15b showed large
578 volume fractions of second-phase particles smaller than 400 nm in the rods extruded

579 at a higher extrusion speed, which would be highly effective to pin grain boundaries
580 to retard grain growth.



581
582 Fig. 14. Optical micrographs of the magnesium alloy rods extruded at a reduction ratio of 29.8,
583 initial billet temperature of 623 K (350 °C) and stem speeds of (a) 0.96, (b) 1.92, (c) 3.93, (d) 6.48
584 and (e) 8.24 mm/s.

585

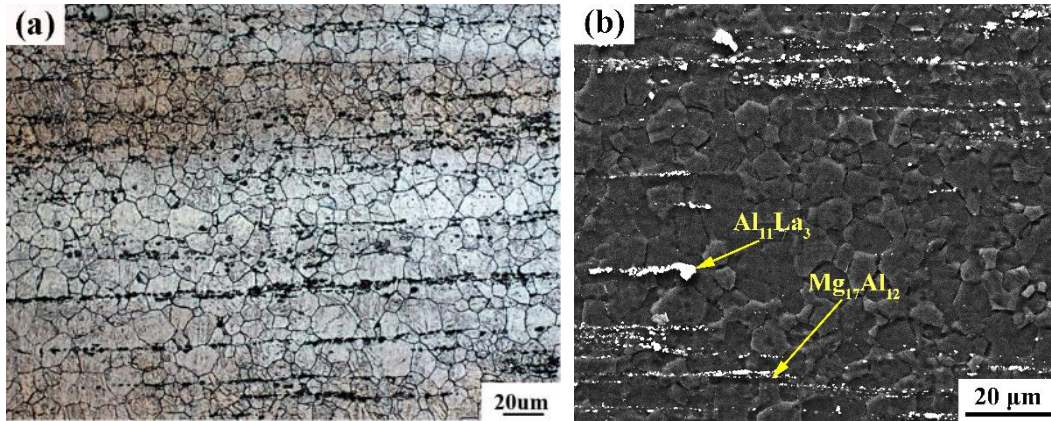


586

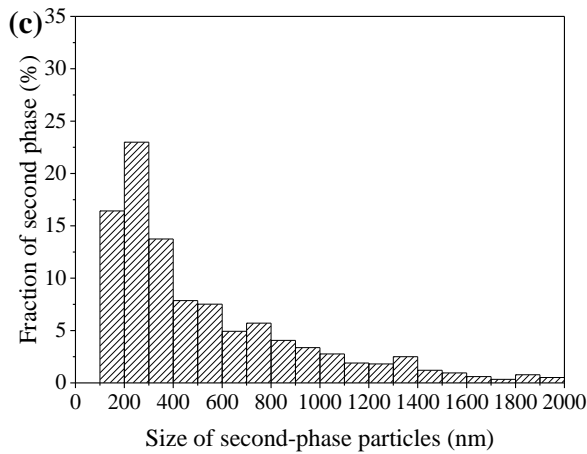
587 Fig. 15 SEM micrograph (a) and distribution of the size of second-phase particles (b) in the rods
 588 extruded at a reduction ratio of 29.8, stem speed of 0.96 mm/s and initial billet temperature of 623
 589 K (350 °C).

590

591 The micrographs of the alloy extruded at the high reduction ratio of 51.0, presented in
 592 Fig. 16, were used to analyze the effect of reduction ratio on the microstructure of the
 593 extruded alloy. The initial billet temperature was 623 K (350 °C) and the stem speed
 594 was 0.96 mm/s. Comparison of the mean grain size obtained from Fig. 16a with that
 595 from Fig. 14a indicated a mild effect of reduction ratio from 29.8 to 51.0 on the mean
 596 grain size (from 8.6 to 9.4 μm). In addition, after extrusion at reduction ratios of 29.8
 597 and 51.0, the volume fractions of second-phase particles were 3.6% and 2.9%,
 598 respectively, as a result of an increase in extrudate temperature.



599

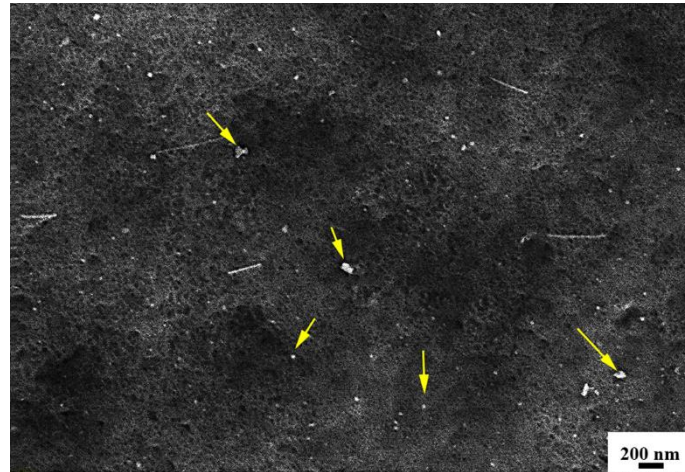


600

601 Fig. 16. Microstructures of the magnesium alloy rods extruded at an initial billet temperature of
 602 623 K (350 °C), stem speed of 0.96 mm/s and reduction ratio of 51.0: (a) optical micrograph; (b)
 603 SEM micrograph; (c) distribution of the sizes of second-phase particles.

604 The size distributions and volume fractions of second-phase particles in Figs. 13, 15
 605 and 16 were determined by using the software Image-Pro Plus on the basis of SEM
 606 micrographs at 2,000X magnification. With this method, nanoscale particles in the
 607 range of 1 and 100 nm were ignored, due to too low resolution. Fig. 17 presents a
 608 SEM micrograph at 20,000X magnification. The observed sample was extruded at an
 609 initial billet temperature of 623 K (250 °C), extrusion speed of 3.93 mm/s and a
 610 reduction ratio of 29.8. Nanoscale particles between 1 and 100 nm marked with

611 arrows are clearly discernible. These tiny particles must have contributed to the
612 improved strength of the extruded magnesium alloy as well, owing to precipitation
613 strengthening.



614
615 Fig. 17 SEM micrograph (20,000X) of the magnesium alloy rod extruded at an initial billet
616 temperature of 523 K (250 °C), extrusion speed of 3.93 mm/s and a reduction ratio of 29.8.

617
618 In the present research, the mean grain sizes of the magnesium rods extruded under all
619 the conditions ranged from 7 to 14 μm . The extrusion condition could influence the
620 mean grain size of the magnesium alloy Mg-Al-Zn-RE to a certain extent, but the
621 influence was quite moderate, in comparison with other magnesium alloys with low
622 alloying contents. Zhang et al. [31], for example, reported that at a reduction ratio of
623 16 and extrusion speed of 4 mm/s, with an increase in billet temperature from 603 K
624 to 673 K (330 °C to 400 °C), the mean grain size of the extruded Mg-1.0Zn-0.5Ca
625 alloy increased from 2.5 μm to 25 μm . The main mechanism governing grain
626 refinement during the hot deformation of a magnesium alloy is dynamic
627 recrystallization (DRX), including the continuous DRX (CDRX) and discontinuous

628 DRX (DDRX) [55, 56]. DDRX, involving the nucleation and growth of new grains,
629 was found to be the predominant mechanism in the magnesium alloy AZ31 [57].
630 Wang et al. [58] demonstrated that a larger value of the Zener-Hollomon parameter
631 resulted in a higher ratio of nucleation rate to growth rate of new grains in the
632 magnesium alloy ZM21, which was helpful for grain refinement. For these
633 magnesium alloys with relatively low alloying contents, extrusion condition was
634 found to influence the grain size of the extrudate strongly.

635

636 For the present magnesium alloy, abundant precipitates were present due to high
637 contents of alloying elements added to magnesium. In addition to extrusion condition,
638 precipitates would influence the DRX behavior of the alloy during extrusion. The
639 precipitated $Mg_{17}Al_{12}$ phase and crushed $Al_{11}La_3$ phase would promote
640 particle-stimulated nucleation (PSN) for DRX. These phases were mostly distributed
641 on grain boundaries to exert the Smith-Zener pinning effect and restrict the growth of
642 DRX grains [38]. Robson et al. [59] demonstrated that coarse, hard second-phase
643 particles in Mg-Mn alloys, which promoted rapid sub-boundary migration during
644 deformation, were necessary for the subsequent occurrence of PSN. Deng et al. [60]
645 found that SiC particles of larger sizes (in the micrometer range) were more effective
646 in promoting PSN of AZ91-SiC composites and refining grains than SiC particles of
647 smaller sizes (in the sub-micrometer range). In the present investigation, second-phase
648 particle sizes increased with increasing initial billet temperature and DRX via PSN

649 would be more important. However, a higher temperature would weaken the
650 nucleation via DDRX. The competition between these two effects made the mean
651 grain size of the present alloy appear to be less sensitive to the initial billet
652 temperature than that of the magnesium alloy Mg-1.0Zn-0.5Ca with low alloying
653 contents [31].

654

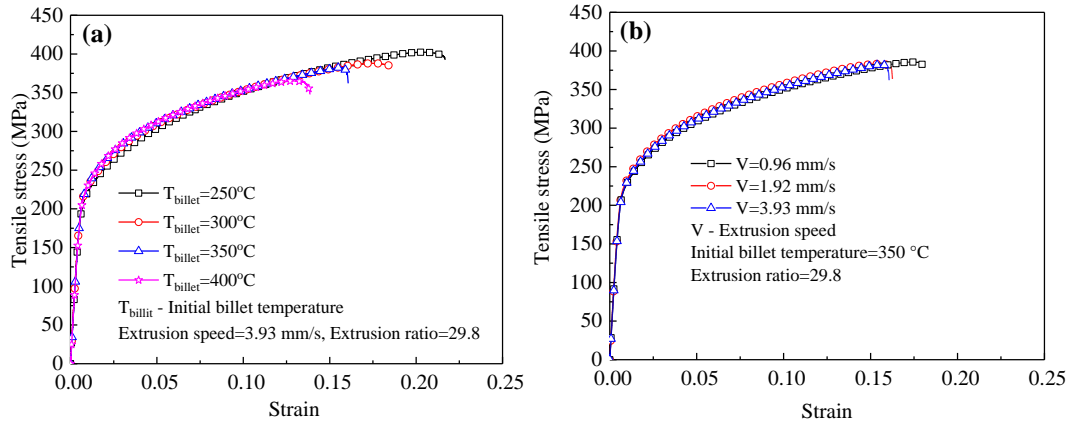
655 As reported earlier, extrusion speed appeared to have a mild influence on the mean
656 grain size of the present magnesium alloy. With increasing extrusion speed, the strain
657 rate of the deforming billet and the extrudate temperature increased. A higher
658 extrudate temperature would promote DRX grain growth, while a high strain rate
659 would restrain DRX grain growth by increasing nucleation rates. As a net result, the
660 direct influence of extrusion speed on the mean grain size became nearly invisible.

661

662 **3.4 Mechanical properties**

663 Fig. 18 shows the tensile stress-strain curves of the magnesium alloy rods extruded at
664 different initial billet temperatures and extrusion speeds. Table 5 lists the tensile
665 properties of the magnesium rods extruded at a reduction ratio of 29.8, together with
666 mean grain sizes. After extrusion at initial billet temperatures of 523, 573, 623 and
667 673 K (250, 300, 350 and 400 °C) and a given stem speed of 3.93 mm/s, the extruded
668 rods had ultimate tensile strengths (UTSs) of 397 ± 7 , 387 ± 1 , 384 ± 3 and 367 ± 7
669 MPa, 0.2% offset yield strengths (YSs) of 217 ± 3 , 220 ± 5 , 221 ± 1 and 221 ± 6 MPa,

670 and elongation values of $20.8 \pm 1.3\%$, $18.2 \pm 0.4\%$, $15.8 \pm 0.4\%$ and $13.6 \pm 0.4\%$,
671 respectively. Clearly, both the UTS and the elongation decreased with rising initial
672 billet temperature, which could be attributed to finer DRX grains at a lower initial
673 billet temperature (Fig. 12 and Table 5). Precipitation strengthening, solid-solution
674 strengthening, dislocation strengthening and subgrain strengthening might have
675 contributed to the strength of the material extruded at a low temperature in addition to
676 fine grain strengthening [38].
677
678 YS, UTS and elongation were only slightly improved by extrusion at a lower
679 extrusion speed. At a given initial billet temperature of 623 K (350 °C), the material
680 extruded at stem speeds of 0.96, 1.92 and 3.93 mm/s had the UTS values of 387 ± 1 ,
681 386 ± 4 and 384 ± 3 MPa, the YS values of 226 ± 4 , 225 ± 8 and 221 ± 1 MPa, and
682 elongation values of $17.0 \pm 1.4\%$, $16.6 \pm 0.5\%$ and $15.8 \pm 0.4\%$, respectively (Table 5).
683 The trends were consistent with the trend of the mean grain size varying with
684 extrusion speed. It means that the scope to control the mean grain size and mechanical
685 properties by varying extrusion speed appeared to be quite limited, which would give
686 freedom to choosing extrusion speed for a higher production rate with only a little
687 effect on the mechanical properties.
688



689
690
691
692

Fig. 18. Tensile stress-strain curves of the magnesium alloy rods extruded (a) at different billet temperatures and (b) at different extrusion speeds.

693 Table 5. Mechanical properties of the rods extruded at a reduction ratio of 29.8.

Stem speed (mm/s)	Billet temperature (°C)	UTS (MPa)	YS (MPa)	Elongation (%)	Mean grain size (μm)
3.93	250	397 ± 7	217 ± 3	20.8 ± 1.3	8.0 ± 0.3
	300	387 ± 1	220 ± 5	18.2 ± 0.4	8.5 ± 0.5
	350	384 ± 3	221 ± 1	15.8 ± 0.4	9.5 ± 0.3
	400	367 ± 7	221 ± 6	13.6 ± 0.4	10.9 ± 0.3
1.92	350	386 ± 4	225 ± 8	16.6 ± 0.5	8.9 ± 0.4
0.96	350	387 ± 1	226 ± 4	17.0 ± 1.4	8.6 ± 0.5

694

695 The ultimate tensile strengths (UTS), yield strengths (YSs) and mean grain sizes of
696 selected Mg alloys are listed in Table 6 for comparison. It can be seen that the present
697 alloy has a mean grain size similar to the mean grain sizes of the magnesium alloys
698 AZ80 [34] and AZ80-1.52La-1.10Gd [61]. However, the present alloy has a higher
699 UTS value than the other magnesium alloys of similar compositions. First of all, an
700 optimized extrusion condition (reduction ratio: 29.8, initial billet temperature: 523 K

701 (250 °C) and ram speed: 3.93 mm/s) was employed to extrude the present alloy.
702 Moreover, the addition of the rare earth elements raises the strengths of magnesium
703 alloys. For example, Jiang et al. [50] found that over a Gd content range of 0.3% to
704 4%, the magnesium alloy AZ80 added with 0.9% Gd exhibited optimum mechanical
705 properties. This was because coarse second phase particles were formed when
706 excessive Gd was added to the magnesium alloy, thereby becoming detrimental to the
707 mechanical properties. Over all, the magnesium alloy with high mechanical properties,
708 both in UTS, YS and elongation, were obtained through adding rare earth elements to
709 AZ80 and extrusion at the optimized condition.

710

711 Magnesium alloys with even finer grains and higher mechanical properties can be
712 prepared through severe plastic deformation (SPD) [62, 63]. For example, Razavi et al.
713 [63] demonstrated that via the multi-temperature (398 K to 473 K, i.e., 125 °C to
714 200 °C) equal-channel angular processing (ECAP) the magnesium alloy AZ31
715 exhibited extraordinarily high mechanical properties (YS = 385 ± 6 MPa, UTS= $455 \pm$
716 4 MPa, elongation=12.7%), owing to the ultra-fine grains (mean grain size= $0.35 \pm$
717 0.10 um) formed during SPD. While the SPD process can significantly improve the
718 mechanical properties of magnesium alloys, this process is only suitable for
719 small-scale material preparation. With the industrial application taken into
720 consideration, the commercial extrusion process may be more advantageous than the
721 SPD process.

722

723

724 Table 6. Yield strengths, ultimate tensile strengths and mean grain sizes of selected

725

Mg alloys for comparison.

Alloy (wt%)	UTS (MPa)	YS (MPa)	Mean grain size (μm)	Extrusion condition		
				Reduction ratio	Initial billet temperature ($^{\circ}\text{C}$)	Ram speed (mm/s)
AZ80 [34]	317-328	200-225	6-8	44	250-350	1
AZ80-1.52La-1.10Gd [61]	304-311	180-225	8.2-13.1	33.6	240-380	2
Mg-3Al-1Zn [63] *	455 \pm 4	385 \pm 6	0.35 \pm 0.10	-	-	-
AZ80-0.2Y-0.2Gd-0.1La [64]	306	264	12 \pm 2	10	380	-
AZ80-1.2Gd-0.8Nd [65]	325	262	-	10	-	-
AZ91-1Ca-0.5Si-0.1La-0.1Ce [66]	318	278	3	30	360	1.45
AZ91-0.3La [67]	330	180	-	17.4	350	1.7
Mg [68]	165	71	33	16.4	350	1.83
Mg-0.2Ce [68]	200-210	-	8	16.4	350	1.83
Mg-3Al [68]	226	105	23	16.4	350	1.83
AZ31 [69]	247	203	23	-	370	-
AM-EX1 [69]	259	184	7	-	370	-
Mg-(0.88-0.96) Mn-(0.32-2.11) Sr [70]	220-250	140-210	35-45	7	350	8
Present alloy (AZ80-1La-0.5Gd)	397 \pm 7	217 \pm 3	8.0 \pm 0.3	29.8	250	3.93

726

* The values were achieved through severe plastic deformation.

727

728 **4. Conclusions**

729

The extrudability and the effects of extrusion process parameters on the

730

microstructure and mechanical properties of a new Mg-Al-Zn-RE alloy with large

731

amounts of alloying elements were investigated by means of extrusion experiments

732

and FE simulations. The following conclusions could be drawn.

733 (1) Hot shortness was the main defect negatively affecting the surface quality
734 of the extruded magnesium alloy. The tendency for hot shortness to occur increased
735 with increasing initial billet temperature, extrusion speed and reduction ratio. The
736 critical temperature for hot shortness to occur was found to be between 754 K and 768
737 K (481 °C and 495 °C).

738 (2) DRX occurred during hot extrusion and grains were significantly refined.
739 The mean grain size of the extruded alloy decreased with decreasing initial billet
740 temperature. An increase in extrusion speed and reduction ratio only slightly
741 promoted DRX grain growth. Fine grains with a mean size of $8.0 (\pm 0.3) \mu\text{m}$ were
742 present in the alloy extruded at an initial billet temperature of 523 K (250 °C), stem
743 speed of 3.93 mm/s and reduction ratio of 29.8.

744 (3) The $\text{Mg}_{17}\text{Al}_{12}$ phase dynamically precipitated during extrusion from the
745 supersaturated magnesium matrix after the solid solution treatment. The $\text{Al}_{11}\text{La}_3$ phase
746 was crushed during extrusion. A large number of second-phase particles with sizes
747 smaller than $1.0 \mu\text{m}$ were distributed on grain boundaries. The volume fraction of
748 second-phase particles decreased with rising extrudate temperature. These particles
749 aided in DRX grain refinement through particle-stimulated nucleation and grain
750 boundary pinning.

751 (4) The UTS and elongation of the extruded rod increased with decreasing initial
752 billet temperature and extrusion speed. The extruded rod with an optimum
753 combination of mechanical properties ($\text{YS}=217 \pm 3 \text{ MPa}$, $\text{UTS}=397 \pm 7 \text{ MPa}$ and

754 elongation=20.8% ($\pm 1.3\%$) was obtained at an initial billet temperature of 523 K
755 (250 °C), stem speed of 3.93 mm/s and reduction ratio of 29.8 mainly as a result of a
756 refined grain structure.

757

758 **Acknowledgements**

759 The authors (Gang Fang and Sheng-Wen Bai) greatly appreciate the financial support
760 of the National Natural Science Foundation of China (Project No.51675300).

761

762 **References**

- 763 [1] M.K. Kulekci, Int. J. Adv. Manuf. Tech., 2008, vol. 39, pp. 851-865.
- 764 [2] A.A. Luo, Int. Mater. Rev., 2004, vol. 49, pp. 13-30.
- 765 [3] E.F. Volkova, Met. Sci. Heat Treat., 2006, vol. 48, pp. 473-478
- 766 [4] S. Yao, Y.F. Li, Sci. Total Environ., 2015, vol. 44, pp. 89-96.
- 767 [5] H. Pan, Y. Ren, H. Fu, H. Zhao, L. Wang, X. Meng, G. Qin, J. Alloy. Compd., 2016,
768 vol. 663, pp. 321-331.
- 769 [6] D. Letzig, J. Swiostek, J. Bohlen, P. A. Beaven, K.U. Kainer, Metal Science J.,
770 2013, vol. 24, pp. 991-996.
- 771 [7] A.A. Luo, J. Magn. Alloy., 2013, vol. 1, pp. 2-22.

- 772 [8] W. A. Monteiro, S. J. Buso, L. V. da Silva, Application of magnesium alloys in
773 transport, in: W.A. Monteiro (Ed.), *New Features on Magnesium Alloys*, InTech,
774 Rijeka, 2012, pp. 1-14.
- 775 [9] S. You, Y. Huang, K.U. Kainer, N. Hort, *J. Magn. Alloys*, 2017, vol. 5, pp.
776 239-253.
- 777 [10]Z. Zeng, N. Stanford, C.H.J. Davies, J.F. Nie, N. Birbilis, *Int. Mater. Rev.*, 2018,
778 vol. 2, pp. 1-36.
- 779 [11]C. Bettles, M. Barnett, *Advances in Wrought Magnesium Alloys: Fundamentals of*
780 *Processing, Properties and Applications*, Woodhead Publishing, Philadelphia, PA,
781 USA, 2012, pp. 304-322.
- 782 [12]D.S. Yin, E.L. Zhang, S.Y. Zeng, *Trans. Nonferr Metal. Soc.*, 2008, vol. 18, pp.
783 763-768.
- 784 [13]W.N. Tang, S.S. Park, B.S. You, *Mater. Des.*, 2011, vol. 32, pp. 3537-3543.
- 785 [14]S. M. Masoudpanah, R. Mahmudi, *Mater. Sci. Eng.*, 2009, vol. A526, pp. 22-30.
- 786 [15]B. Zhang, Y. Wang, L. Geng, C. Lu, *Mater. Sci. Eng. A*, 2012, vol. 539, pp. 56-60.
- 787 [16]J. Bohlen, S. Yi, D. Letzig, K.U. Kainer, *Mater. Sci. Eng. A*, 2010, vol. 527, pp.
788 7092-7098.
- 789 [17]D.K. Xu, W.N. Tang, L. Liu, Y.B. Xu, E.H. Han, *J. Alloy. Compd.*, 2007, vol. 432,
790 pp. 129-134.
- 791 [18]D.K. Xu, L. Liu, Y.B. Xu, E.H. Han, *J. Alloy. Compd.*, 2006, vol. 426, pp. 155-161.
- 792 [19]N. Stanford, M. R. Barnett, *Mater. Sci. Eng. A*, 2008, vol. 496, pp. 399-408.

- 793 [20]M. Yamasaki, K. Hashimoto, K. Hagihara, Y. Kawamura, *Acta Mater.*, 2011, vol.
794 59, pp. 3646-3658.
- 795 [21]X. Li, W. Qi, K. Zheng, N. Zhou, *J. Magn. Alloys*, 2013, vol. 1, pp. 54-63.
- 796 [22]X. Zeng, Y. Zhang, C. Lu, W. Ding, Y. Wang, Y. Zhu, *J. Alloy. Compd.*, 2005, vol.
797 395, pp. 213-219.
- 798 [23]N. Stanford, D. Atwell, M. R. Barnett, *Acta Mater.*, 2010, vol. 58, pp. 6773-6783.
- 799 [24]J.B. Zhang, L.B. Tong, C. Xu, Z.H. Jiang, L.R. Cheng, S. Kamado, H.J. Zhang,
800 *Mater. Sci. Eng. A*, 2017, vol. 708, pp. 11-20.
- 801 [25]T. Homma, N. Kunito, S. Kamado, *Scripta Mater.*, 2009, vol. 61, pp. 644-647.
- 802 [26]M. Yamasaki, T. Anan, S. Yoshimoto, Y. Kawamura, *Scripta Mater.*, 2005, vol. 53,
803 pp. 799-803.
- 804 [27]Y. Chen, L. Hao, Y. Ruiyu, G. Liu, T. Xia, *Mater. Sci. Technol.*, 2014, vol. 30, pp.
805 495-500.
- 806 [28]A. A. Luo, C. Zhang, A. K. Sachdev, *Scripta Mater.*, 2012, vol. 66, pp. 491-494.
- 807 [29]T. Murai, S.I. Matsuoka, S. Miyamoto, Y. Oki, *J. Mater. Process. Technol.*, 2001,
808 vol. 141, pp. 207-212.
- 809 [30]S. Ishihara, H. Shibata, K. Komano, T. Goshima, Z.Y. Nan, *Key Eng. Mater.*, 2007,
810 vol. 353, pp. 291-294.
- 811 [31]B.P. Zhang, L. Geng, L.J. Huang, X.X Zhang, C.C. Dong, *Scripta Mater.*, 2010, vol.
812 63, pp. 1024-1027.

- 813 [32]L.B. Tong, M.Y. Zheng, L.R. Cheng, D.P. Zhang, S. Kamado, J. Meng, H.J. Zhang,
814 Mater. Charact., 2015, vol. 104, pp. 66-72.
- 815 [33]S.H. Park, J.G. Jung, Y.M. Kim, B.S. You, Mater. Lett., 2015, vol. 139, pp. 35-38.
- 816 [34]M. Shahzad, L. Wagner, Mater. Sci. Eng. A, 2009, vol. 506, pp. 141-147.
- 817 [35]Q. Chen, D. Shu, Z. Zhao, Z. Zhao, Y. Wang, B. Yuan, Mater. Des., 2012, vol. 40,
818 pp. 488-496.
- 819 [36]A. Singh, Y. Osawa, H. Somekawa, H. Somekawa, T. Mukai, C.J. Parrish, D.S.
820 Shih, Metall. Mater. Trans. A, 2014, vol. 45, pp. 3232-3240.
- 821 [37]S.H. Park, J.H. Bae, S.H. Kim, J. Yoon, B.S. You, Metall. Mater. Trans. A, 2015,
822 vol. 46, pp. 5482-5488.
- 823 [38]F. Bu, Q. Yang, K. Guan, X. Qiu, D. Zhang, W. Sun, J. Alloy. Compd., 2016, vol.
824 688, pp. 1241-1250.
- 825 [39]X. Luo, S. Dang, L. Kang, Adv. Mater. Sci. Eng., 2014, vol. 2014, pp. 1-7.
- 826 [40]J. Mohammadi, M. Ghoreishi, Y. Behnamian, Mater. Res., 2014, vol. 17, pp.
827 994-1002.
- 828 [41]C.M. Sellars, W.J. McTegart, Acta Metall., 1966, vol. 14, pp. 1136-38
- 829 [42]L. Li, H. Zhang, J. Zhou, J. Duszczyk, G. Li, Z.H. Zhong, Mater. Des., 2008, vol.
830 29, pp. 1190-1198.
- 831 [43]G. Liu, J. Zhou, J. Duszczyk, J. Mater. Process. Technol., 2008, vol. 200, pp.
832 185-198.

- 833 [44]L. Li, J. Zhou, and J. Duszczyk, *J. Mater. Process. Technol.*, 2006, vol. 172, pp.
834 372–80.
- 835 [45]J. Zhou, L. Li, J. Duszczyk, *J. Mater. Process. Technol.*, 2003, vol. 134, pp.
836 383-397.
- 837 [46]T. Sheppard, *Extrusion of Aluminum Alloys*, Kluwer Academic Publishers,
838 Dordrecht, The Netherlands, 1999, pp. 227–52.
- 839 [47]M.P. Clade, T. Sheppard, *Mater. Sci. Technol.*, 1993, vol. 9, pp. 313-318.
- 840 [48]W. Wei, C. Xu, J. Zhang, X. Niu, *China Foundry*, 2014, vol. 11, pp. 157-162.
- 841 [49]Y.S. Yang, J.C. Wang, T. Wang, C.M. Liu, Z.M. Zhang, *Trans. Nonferr Metal. Soc.*,
842 2014, vol. 24, pp. 76-81.
- 843 [50]N. Jiang, L.G. Meng, X.G. Zhang X G, L. Chen, C.F. Fang, H. Hao, *Rare Met.*,
844 2017, pp. 1-7.
- 845 [51]X.D. Wang, W.B. Du, K. Liu, Z.H. Wang, S.B. Li, *J. Alloys Comp.*, 2012, vol. 522,
846 pp. 78– 84.
- 847 [52]J.C. Wurst, J.A. Nelson, *J. Am. Ceram. Soc.*, 1972, vol. 55, pp. 109-109.
- 848 [53]H. Ding, L. Liu, S. Kamado, D. Wang, Y. Kojima, *J. Alloy. Compd.*, 2008, vol. 456,
849 pp. 400-406.
- 850 [54]S.W Xu, N. Matsumoto, S. Kamado, T. Honma, Y. Kojima, *Scripta Mater.*, 2009,
851 vol. 61, pp. 249-252.
- 852 [55]S.M. Fatemi-Varzaneh, A. Zarei-Hanzaki, H. Beladi, *Mater. Sci. Eng. A*, 2007, vol.
853 456, pp. 52-57.

- 854 [56]O. Sitdikov, R. Kaibyshev, *Mater. Trans.*, 2001, vol. 42, pp. 1928-1937.
- 855 [57]A.G. Beer, M.R. Barnett, *Metall. Mater. Trans. A*, 2007, vol. 38, pp. 1856-1867.
- 856 [58]L. Wang, G. Fang, L. Qian, *Mater. Sci. Eng. A*, 2018, vol. 711, pp. 268-283.
- 857 [59]J.D. Robson, D.T. Henry, B. Davis, *Acta Mater.*, 2009, vol. 57, pp. 2739-2747.
- 858 [60]K.K. Deng, X.J. Wang, Y.W. Wu, X.S. Hu, K. Wu, W.M. Gan, *Mater. Sci. Eng. A*,
859 2012, vol. 543, pp. 158-163.
- 860 [61]Q. Liao, X. Chen, Q. Lan, F. Ning, Q. Le, *Mater. Res. Express*, 2018, vol. 5, pp.
861 1-10.
- 862 [62]D.C. Foley, M. Al-Maharbi, K.T. Hartwig, I. Karaman, L.J. Kecskes, S.N.
863 Mathaudhu, *Scripta Mater.*, 2011, vol. 64, pp. 193-196.
- 864 [63]S.M. Razavi, D.C. Foley, I. Karaman, K.T. Hartwig, O. Duygulu, L.J. Kecskes,
865 S.N. Mathaudhu, V.H. Hammond, *Scripta Mater.*, 2012, vol. 67, pp. 439-442.
- 866 [64]K. Cai, Z. Gao, Q. Zhu, Y. Jin, Y. Chai, D. Fang, *Rare Metal Mater. Eng.*, 2015, vol.
867 44, pp. 1489-1493.
- 868 [65]Q. Zhu, C. Fang, N. Li, L. Meng, Y. Wang, Y. Wu, X. Zhang, *Rare Metal Mater.*
869 *Eng.*, 2013, vol. 42, pp. 771-775.
- 870 [66]C. Che, Z. Cai, X. Yang, L. Cheng, Y. Du, *Mater. Sci. Eng. A*, 2017, vol. 705, pp.
871 282-290.
- 872 [67]L. Fu, X.B. Wang, P.L. Gou, Q.C. Le, W. T. Jia, Y. Tang, *Adv. Eng. Mater.*, 2017,
873 vol. 19, pp. 1700230.

- 874 [68] A.A. Luo, W. Wu, R.K. Mishra, L. Jin, A.K. Sachdev, W. Ding, *Metall. Mater.*
875 *Trans. A*, 2010, vol. 41, pp. 2662-2674.
- 876 [69] M. Easton, A. Beer, M. Barnett, C. Davies, G. Dunlop, Y. Durandet, S. Blacket, T.
877 Hilditch, P. Beggs, *JOM*, 2008, vol. 60, pp. 57-62.
- 878 [70] H. Borkar, M. Hoseini, M. Pekguleryuz, *Mater. Sci. Eng. A*, 2012, vol. 549, pp.
879 168-175.

880 **Table and figure captions**

- 881 Table 1. Nominal chemical composition (wt.%) of the Mg-Al-Zn-RE alloy.
- 882 Table 2. Constitutive constants of the magnesium alloy (Mg-Al-Zn-RE).
- 883 Table 3. Physical properties of the billet and extrusion tooling.
- 884 Table 4. EDS analysis of second-phase particles in the as-cast alloy.
- 885 Table 5. Mechanical properties of the rods extruded at a reduction ratio of 29.8.
- 886 Table 6. Yield strengths, ultimate tensile strengths and mean grain sizes of selected
887 Mg alloys for comparison.
- 888
- 889 Fig. 1. Flow stress curves of the magnesium alloy at temperatures from 773 K to 693
890 K (300 °C to 420 °C) and strain rates (a) 0.001 s⁻¹, (b) 0.01 s⁻¹, (c) 0.1 s⁻¹, (d) 1 s⁻¹ and
891 (e) 10 s⁻¹.

892 Fig. 2. Tooling set-up to extrude rods: (a) schematic and (b) dimensions of one of the
893 extrusion dies.

894 Fig. 3. Schematic of the longitudinal section of an extruded rod for microstructure
895 observation.

896 Fig. 4. Axisymmetric FE model to simulate the extrusion process to produce rods.

897 Fig. 5. Predicted temperature distribution inside the billet, extrudate and extrusion
898 tooling (a) and comparison between the measured and predicted temperatures at P1
899 along with stem displacement (b).

900 Fig. 6. FE simulated temperature evolutions at point P2 during extrusion: (a) at a
901 reduction ratio of 29.8, stem speed of 3.93 mm/s and different initial billet
902 temperatures, (b) at a reduction ratio of 29.8, initial billet temperature of 623 K
903 (350 °C) and different stem speeds, and (c) at a reduction ratio of 51.0, initial billet
904 temperature of 623 K (350 °C) and different stem speeds.

905 Fig. 7. Simulated temperatures at point P2 with friction factor values of 0 and 1.

906 Fig. 8. Magnesium alloy rods extruded at a reduction ratio of 29.8, stem speed of 3.93
907 mm/s and different billet temperatures. (a) $T=523$ K (250 °C) and $T_e=702$ K (429 °C);
908 (b) $T=573$ K (300 °C) and $T_e=723$ K (450 °C); (c) $T=623$ K (350 °C) and $T_e=749$ K
909 (476 °C); (d) $T=673$ K (400 °C) and $T_e=769$ K (496 °C); (e) $T=713$ K (440 °C) and
910 $T_e=793$ K (520 °C). T_e is the maximum extrudate temperature.

911 Fig. 9. Magnesium alloy rods extruded at a reduction ratio of 29.8, initial billet
912 temperature of 623 K (350 °C) and different stem speeds. (a) $v=0.96$ mm/s and
913 $T_e=674$ K (401 °C); (b) $v=1.92$ mm/s and $T_e=712$ K (439 °C); (c) $v=3.93$ mm/s and
914 $T_e=749$ K (476 °C); (d) $v=6.48$ mm/s and $T_e=768$ K (495 °C); (e) $v=8.24$ mm/s and
915 $T_e=787$ K (514 °C). T_e is the maximum extrudate temperature.

916 Fig. 10. Magnesium alloy rods extruded at a reduction ratio of 51.0, initial billet
917 temperature of 623 K (350 °C) and different stem speeds. (a) $v=0.96$ mm/s and
918 $T_e=690$ K (417 °C); (b) $v=1.92$ mm/s and $T_e=733$ K (460 °C); (c) $v=3.07$ mm/s and
919 $T_e=754$ K (481 °C); (d) $v=3.93$ mm/s and $T_e=779$ K (506 °C); (e) $v=5.39$ mm/s and
920 $T_e=786$ K (513 °C). T_e is the maximum extrudate temperature.

921 Fig. 11. Microstructures of the Mg-Al-Zn-RE alloy: (a) dendritic structure of the
922 as-cast alloy; (b) equiaxed grain structure of the solid-solution-treated alloy; (c) SEM
923 micrograph of the as-cast alloy; (d) SEM micrograph of the solid-solution treated
924 alloy; (e-h) EDS element maps of Al_2Gd , $Al_{11}La_3$, $Mg_{17}Al_{12}$ and Al_8Mn_5 phases.

925 Fig. 12. Optical micrographs of the magnesium alloy rods extruded at a reduction
926 ratio of 29.8, stem speed of 3.93 mm/s and initial billet temperatures of (a) 523, (b)
927 573, (c) 623, (d) 673 and (e) 713 K [(a) 250, (b) 300, (c) 350, (d) 400 and (e) 440 °C].

928 Fig. 13. SEM micrographs and distributions of the sizes of second-phases particles in
929 the rods extruded at a reduction ratio of 29.8, stem speed of 3.93 mm/s and initial
930 billet temperatures of (a) (c) 523 K (250 °C) and (b) (d) 623 K (350 °C).

931 Fig. 14. Optical micrographs of the magnesium alloy rods extruded at a reduction
932 ratio of 29.8, initial billet temperature of 623 K (350 °C) and stem speeds of (a) 0.96,
933 (b) 1.92, (c) 3.93, (d) 6.48 and (e) 8.24 mm/s.

934 Fig. 15. SEM micrograph (a) and distribution of the size of second-phase particles (b)
935 in the rods extruded at a reduction ratio of 29.8, stem speed of 0.96 mm/s and initial
936 billet temperature of 623 K (350 °C).

937 Fig. 16. Microstructures of the magnesium alloy rods extruded at an initial billet
938 temperature of 623 K (350 °C), stem speed of 0.96 mm/s and reduction ratio of 51.0:
939 (a) optical micrograph; (b) SEM micrograph; (c) distribution of the sizes of
940 second-phase particles.

941 Fig. 17. SEM micrograph (20,000X) of the magnesium alloy rod extruded at an initial
942 billet temperature of 523 K (250 °C), extrusion speed of 3.93 mm/s and a reduction
943 ratio of 29.8.

944 Fig. 18. Tensile stress-strain curves of the magnesium alloy rods extruded (a) at
945 different billet temperatures and (b) at different extrusion speeds.